



UNIVERSITÀ DI PISA

Dipartimento di Ingegneria dell'Energia, dei Sistemi, del
Territorio e delle Costruzioni
Corso di Laurea Magistrale in Ingegneria Elettrica

Electromagnetic and thermal analysis of a permanent magnet synchronous motor

Candidato:

Gabriele Montinaro

Relatore:

Prof. Luca Sani

Anno Accademico 2015-2016

Acknowledgements

From the first moment in the *Fraunhofer LBF*, I have felt a member of a young and hungry team and for this reason there are so many people to thank.

Foremost I would like to express my deep gratitude to my German supervisor *Alexander Dautfest* of the TU Darmstadt, for the useful recommendations, for the German lessons and for encouragement whenever i ran into a trouble spot.

I would like to offer my special thanks to Professor *Luca Sani* of University of Pisa for giving the opportunity of this thesis.

I offer my sincere appreciation to Dipl.-Ing. *Rüdiger Heim*, the director of ZSZ-e center, for his warm welcome in the team.

I am particularly grateful to MSc *Marcel Lehr* of TU Darmstadt and to Dipl.Ing.*Mehran Mirazei* of Powersys for giving me the useful lessons about the JMag software.

German lessons of Prof. *Christina Braun* provided me the basic knowledges about the language and life in Germany.

I would also like to extend my thanks to Dipl. Ing. *David Flaschenträger* for accepting me in the team.

I thank my fellow labmates in Fraunhofer LBF for the support and for the fantastic experiences spent together. In particular, thank to *Florian Besthorn*, for his patience and for his constructive suggestions.

Last but not the least, I would like to thank the *Italian crew* in Fraunhofer, that with a simple “caffè” they were able to turn cloudy days into sunny days.

Contents

- Acknowledgements III
- Abbreviations and Variables VI
- List of Figures..... VII
- List of Tables IX
- 1 Introduction..... - 1 -**
- 1.1 Permanent Magnets - 2 -
- 1.2 PMSM - 9 -
- 1.3 Mathematical Model - 11 -
- 1.3.1 Direct and Quadrature Axis Inductances - 16 -
- 1.4 Scientific Contribution - 17 -
- 2 Motor Characteristics and Sizing..... - 18 -**
- 2.1 Motor Design..... - 19 -
- 2.2 Winding..... - 22 -
- 2.2.1 Stator Winding Design - 23 -
- 2.3 Winding Stator Resistance - 29 -
- 2.4 Losses - 30 -
- 3 FE Analysis..... - 35 -**
- 3.1 2D Model..... - 36 -
- 3.1.1 Material - 38 -
- 3.2 Circuit..... - 41 -
- 3.2.1 Alignment of the Rotor with the Stator - 41 -
- 3.3 Nominal Point - 43 -
- 3.3.1 Inductances of Direct and Quadrature axis - 44 -
- 3.4 Maximum Torque..... - 45 -
- 3.5 Post Process-Iron Loss study..... - 46 -
- 3.6 Efficiency Map..... - 47 -
- 3.7 FE Analysis of Losses as a Function of Current Phase Angle - 52 -
- 3.7.1 Simulation Results..... - 53 -
- 4 Thermal Analysis - 58 -**
- 4.1 Mechanisms of Heat Transfer- Conduction - 59 -
- 4.1.1 Convection - 59 -
- 4.1.2 Heat Storage - 60 -
- 4.2 General Cylindrical Component..... - 60 -
- 4.3 Lumped Parameter Thermal Network..... - 61 -
- 4.3.1 Frame and Cooling Jacket - 63 -
- 4.3.2 Stator Yoke..... - 66 -
- 4.3.3 Stator Teeth - 67 -
- 4.3.4 Stator Winding - 68 -

4.3.5	Airgap.....	- 69 -
4.3.6	Permanent Magnets	- 70 -
4.3.7	Rotor.....	- 71 -
4.3.8	Shaft	- 72 -
4.4	Steady-State Analysis.....	- 73 -
4.5	Transient Analysis	- 74 -
4.6	Results	- 74 -
5	Summary.....	- 78 -
	Bibliography	- 80 -
	Appendix	- 83 -
	A Efficiency Map- Matlab Code	- 83 -
	B Thermal Resistances	- 84 -

Abbreviations and Variables

Symbols

B	Magnetic flux density
C	Clarke Matrix
C_c	Curie constant
H	Magnetic intensity field
I	Current
L_d	Direct axis Inductance
L_q	Quadrature axis inductance
M	Material magnetization
m	Number of phases
N	Number of turns
n	Revolution speed in rpm
P	Park Matrix
p	Number of pole pairs
Q	Number of Stator slots
q	Number of slots per pole and per phase
T_c	Curie temperature
U	Voltage

Acronyms

EV	Electric Vehicles
PM	Permanent Magnet
PMSM	Permanent Magnet Synchronous Machine
IPMSM	Interior Permanent Magnet Synchronous Machine
SPMSM	Surface Mounted Permanent Magnet Synchronous Machine
RMS	Root Mean Square
Mmf	Magneto motive force
LPTN	Lumped Parameter Thermal Network

Greek letters

α_r	Temperature coefficient of resistance
λ	Thermal conductivity
δ	Airgap
Ψ	Flux linkage
\mathcal{R}	Reluctance
θ	Temperature
Φ_{wc}	Wire Conductor Diameter
ζ	Steinmetz constant

List of Figures

Figure 1 Price trend for Neodymium and Dysprosium [1] - 1 -

Figure 2 Intrinsic and normal B-H curves..... - 3 -

Figure 3 Magnetic open circuit - 4 -

Figure 4 PM operating point - 5 -

Figure 5 Magnetic circuit with current..... - 5 -

Figure 6 Operating point with armature current..... - 6 -

Figure 7 Ferromagnetic below T_c - 7 -

Figure 8 Paramagnetic above T_c - 7 -

Figure 9 B-H curves depending on temperature - 7 -

Figure 10 B-H normal curves of different PMs - 8 -

Figure 11 Impact of temperature on N33H (Source: Arnold Magnetics) - 10 -

Figure 12 Different configurations of PMSM..... - 11 -

Figure 13 A simplified representation of a three-phase PMSM..... - 11 -

Figure 14 Clarke Transformation..... - 13 -

Figure 15 Park Transformation - 14 -

Figure 16 Phasor Diagram PMSM..... - 15 -

Figure 17 Magnet-Reluctance Torque..... - 15 -

Figure 18 a) SPSM Isotropic b) IPMSM Anisotropic [4] - 17 -

Figure 19 Torque-Speed curve of the motor (Internal source)..... - 19 -

Figure 20 Explosion of the motor components - 20 -

Figure 21 PM radial magnetization - 21 -

Figure 22 Motor CAD - 21 -

Figure 23 Coil..... - 22 -

Figure 24 Double-layer windings..... - 22 -

Figure 25 Slot fill factor - 23 -

Figure 26 Voltage phasor diagram - 25 -

Figure 27 Sector of star of slots - 26 -

Figure 28 Coil span - 27 -

Figure 29 Phasor diagram - 29 -

Figure 30 Four-terminal sensing - 30 -

Figure 31 Eddy current path..... - 33 -

Figure 32 2D Model mesh..... - 37 -

Figure 33 Radial division of the airgap mesh	- 37 -
Figure 34 Normal Curve of Neomax 37SH (Source: Hitachi Metals).....	- 38 -
Figure 35 Magnetization curve of NO20 at 50Hz.....	- 39 -
Figure 36 Specific loss B (f)	- 40 -
Figure 37 Electric circuit.....	- 41 -
Figure 38 Rotor position respect stator reference uvw	- 42 -
Figure 39 No-load voltage.....	- 43 -
Figure 40 Nominal torque	- 43 -
Figure 41 Inductance depending on electrical angle.....	- 45 -
Figure 42 Rotor	- 45 -
Figure 43 Maximum torque.....	- 45 -
Figure 44 7 Points efficiency map.....	- 48 -
Figure 45 Efficiency map	- 51 -
Figure 46 Phasor diagram with $I_d=0$	- 52 -
Figure 47 Phasor diagram with $I_d \neq 0$	- 53 -
Figure 48 Torque depend on current β ($n=4000$ rpm; $I=255A_{rms}$).....	- 54 -
Figure 49 Rotor Iron Losses depend on β	- 54 -
Figure 50 Stator Iron Losses depend on β	- 55 -
Figure 51 PM Losses depend on β	- 55 -
Figure 52 Overall losses regarding on the β angle.....	- 56 -
Figure 53 Overall losses vs Torque regarding on the β	- 57 -
Figure 54 Thermal network-cylindrical component.....	- 61 -
Figure 55 Thermal network.....	- 62 -
Figure 56 Cooling channel	- 64 -
Figure 57 Stator yoke	- 66 -
Figure 58 Stator teeth	- 67 -
Figure 59 Detail of stator slot.....	- 68 -
Figure 60 Equivalent stator winding	- 69 -
Figure 61 Rotor 2D	- 71 -
Figure 62 Hole radius	- 72 -
Figure 63 Transient state temperatures ($\beta=90^\circ$).....	- 76 -
Figure 64 Transient state temperatures ($\beta=110^\circ$).....	- 76 -

List of Tables

Table 1 Main propriety of hard magnetic materials [2]	- 8 -
Table 2 Maximum operating temperature NdFeB	- 9 -
Table 3 Motor Characteristics (Internal Source).....	- 18 -
Table 4 Motor characteristics (Internal source)	- 18 -
Table 5 Wire parameter.....	- 23 -
Table 6 Slot geometry	- 23 -
Table 7 Star of slots parameter.....	- 24 -
Table 8 spokes number configuration	- 25 -
Table 9 Emf value	- 27 -
Table 10 Windings configuration.....	- 27 -
Table 11 Algebraic sum of phasor for top and bottom layer	- 28 -
Table 12 NO20 Physical Proprieties	- 39 -
Table 13 Magnetization curve of NO20 at 50Hz	- 39 -
Table 14 Specific total loss for hysteresis depending on B and frequency.....	- 40 -
Table 15 FFT No-Load voltage.....	- 42 -
Table 16 Inductance table	- 44 -
Table 17 Punching factor	- 46 -
Table 18 Magnet correction factor	- 47 -
Table 19 7 Operating points for efficiency map	- 48 -
Table 20 7 Operating points: power losses	- 49 -
Table 21 Interpolation coefficients	- 49 -
Table 22 Torque as a function of current phase angle (n=4000 rpm; I=255A _{rms})	- 53 -
Table 23 Iron Losses depend on β (n=4000rpm; I=255A _{rms}).....	- 54 -
Table 24 Losses depend on current phase angle (n=4000 rpm; I=255A _{rms})	- 56 -
Table 25 Comparison of results	- 57 -
Table 26 Analogy between thermal and electric circuit.....	- 58 -
Table 27 Thermal nodes	- 59 -
Table 28 Component explanation of the thermal network.....	- 63 -
Table 29 Physical properties of water at different temperatures.....	- 64 -
Table 30 Fluid dynamic parameter of Cooling Jacket	- 65 -
Table 31 NO20 physical proprieties.....	- 67 -
Table 32 Winding thermal proprieties	- 69 -

Table 33 Air physical proprieties at 50°	- 70 -
Table 34 NdFeB physical proprieties.....	- 71 -
Table 35 Shaft physical proprieties	- 73 -
Table 36 Steady state results ($\beta=90^\circ$).....	- 75 -
Table 37 Steady state results ($\beta=110^\circ$).....	- 75 -
Table 38 Comparison of temperature results	- 77 -

1 Introduction

Decreasing the concentration of CO₂ in the atmosphere is one of the main challenges of the Twenty-First century. Electric vehicles (EV) could be an efficient solution for the purpose.

The motors used in the electric drive trains are typically of two typologies: induction and permanent magnet synchronous machines (PMSM). In PMSM, the excitation field is provided by the permanent magnets (*PM*) in the rotor instead of coils. Therefore, the excitation windings are not present in the PMSM. It implicates a reduction of losses, and overall weight, thus gaining high efficiency and high power density.

The progress of power electronics and the employment of rare earth elements have increased the development of this typology. New components are introduced during the manufacturing process of *PMs* in order to increase the performances. For instance, Dysprosium is able to increase the thermal stability. Such component is added during the realization of Neodymium Iron Boron, which is currently the most promising magnetic material in high power applications.

However, the high costs of rare earth materials pose a threat to the economic attainability and the growth of the electric vehicle market.

During the last years, the price of the Dysprosium has increased significantly, as shown in the Figure 1. Therefore, its employment must be reduced for saving money. It is possible by decreasing the *PMs* operating temperature.

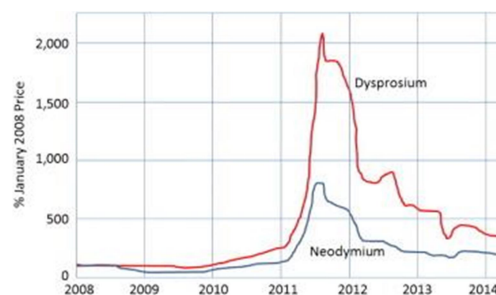


Figure 1 Price trend for Neodymium and Dysprosium [1]

In order to reduce the working temperature, a complete analysis of the power losses in the motor is needed, since they represent the heat sources.

The influence of rotational speed and amplitude of the current on heat generation must be evaluated.

Within the project KSE, developed at *Fraunhofer Institute Lbf*; different research facilities investigate the possibility to reduce the need of rare earth materials for electric motors.

The intent of this work is the evaluation of possible reduction power losses and the thermal behaviour of the system.

The manuscript is organized as follows: first an introduction of PMs and some consideration regarding the *Neodymium Iron Boron*. Moreover, a mathematical model of PMSM is illustrated. Next, a geometrical, electrical and mechanical description of the motor is shown. Given that, the number of slots per pole per phase (q) is not an integer, an accurate study of the winding configuration is performed.

Afterwards, the power budget analysis is executed and the reduction of iron losses by FEM model is evaluated.

Finally, by a lumped parameter thermal network the thermal analysis is conducted and the steady-state temperature is calculated as a function of the current phase angle.

To evaluate the magnetic state in the different case and then the power losses, the finite element software *JMag* is used. For the winding design and for the temperature evaluation, a Spreadsheet and *Dymola* are employed.

1.1 Permanent Magnets

Ferromagnetic materials are divided into two categories: soft and hard materials. These last materials retain their magnetism even without an external magnetic field. Permanent magnets (PMs) are composed with hard ferromagnetic materials.

Initially, these materials consist of magnetic domains (*Weiss domains*) with random orientation such that the overall magnetization is zero. When an external magnetic field H is applied to these domains, they turn parallel to the direction of the magnetic field and they create an own magnetic polarization M . This polarization amplifies the external field, yielding a resulting magnetic flux density (1):

$$B = \mu_0(H + M) \quad (1)$$

Where $\mu_0 = 4\pi \cdot 10^{-7} H/m$ is the vacuum permeability and the magnetization M is given by Eq. (2):

$$M = \mu_0(\mu_r - 1)H = \chi_m H \quad (2)$$

μ_r is the relative permeability associated with the material and χ_m is the material susceptibility. Depending on the value of the χ_m the magnetic materials are classified in: *diamagnetic* ($\chi_m < 0$), *paramagnetic* ($\chi_m > 0$) and *ferromagnetic* ($\chi_m \gg 0$).

The performances of ferromagnetic materials are characterized by the B - H curve, or *hysteresis* loop, shown in Figure 2. The dotted curves represent the first magnetization or “*virgin*”

curves. When all domains are in parallel with the external field, the maximum value of magnetization ($M=M_s$), also known as *saturation* (point *e*) is achieved.

In Figure 2, drawn are the intrinsic curve (black) and the normal curve (red). The first one characterizes the magnetic flux density that the material produces ($M-H$). The second one is the magnetic flux density due to the combination of the air and the material ($B-H$).

The interest points of the curves are:

- *Coercive field strength* (H_c): is the magnetic field intensity necessary to bring the magnetic flux density to zero (point *g*).
- *Remanence magnetic flux density* (B_r): is the residual magnetic flux density corresponding to zero magnetic field intensity (point *f*).

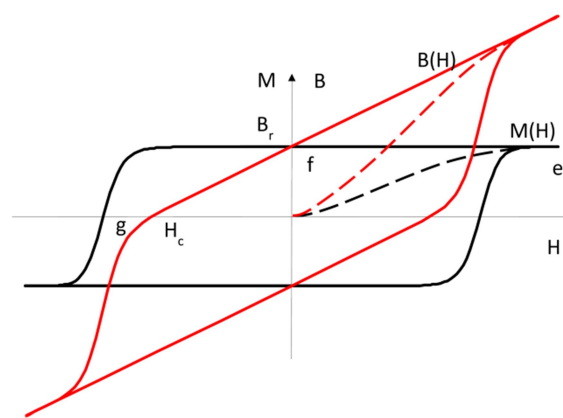


Figure 2 Intrinsic and normal B-H curves

The second quadrant represents the conditions where the *PM* works in practice. The corresponding curve is called the *demagnetization curve*.

For the permanent magnet is also defined a quality factor called the *Maximum energy product* (BH_{max}). When a magnetic circuit is realized to work at the BH_{max} point, the magnet volume is reduced to its smallest value. Geometrically it is represented by the maximum rectangular area that can be inscribed under the normal curve.

The main differences between hard and soft magnetic materials are the area of the hysteresis loop and the relative permeability. Hard materials present a wider hysteresis loop and a high coercive magnetic field.

Operating Point of PM

The operating point of PM material is important in order to avoid the irreversible demagnetization. This happens when the reverse magnetic field is strong enough and therefore, the operating point is located below the “*knee*” in the BH -curve.

For evaluating this point, an elementary magnetic circuit is studied. Figure 3 shows the permanent magnet (*red*) introduced in the magnetic circuit consisting of iron (*blue*) and an air gap. Moreover, the black arrow represents the PM magnetization direction.

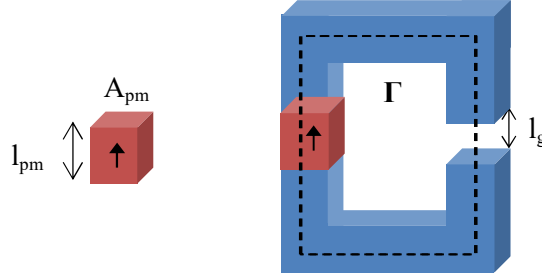


Figure 3 Magnetic open circuit

The subscript *pm* and *g* correspond to permanent magnet and airgap respectively, *l* is the length and *A* is the cross sectional area.

With the assumption of iron permeability much higher than the permeability of PM and air ($\mu_{fe} \rightarrow \infty$), the iron contributions can be neglected.

Starting from the *Ampere's* law for a closed flux line Γ , the sum of the magneto-motive force (*mmf*) generated by the PM and the mmf received by the air gap is zero:

$$\oint_{\Gamma} \vec{H} \cdot d\vec{l} = H_{pm}l_{pm} + H_g l_g = 0 \quad (3)$$

Neglecting the leakage fluxes, from the *Gauss's* law, the magnetic flux density is given by Eq. (4):

$$B_{pm}A_{pm} - B_g A_g = 0 \quad (4)$$

The magnetic field intensity of the PM can be defined as (5):

$$H_{pm} = -\frac{H_g l_g}{l_{pm}} \quad (5)$$

The permanent magnetic flux density is expressed by Eq.(6):

$$B_{pm} = \frac{B_g A_g}{A_{pm}} \quad (6)$$

The magnetic field intensity is related to the air gap flux density by Eq. (7):

$$H_g = \frac{B_g}{\mu_0} \quad (7)$$

Combining the equations, the magnetic flux density in the PM can be defined as:

$$B_{pm} = -\mu_0 \frac{l_{pm} A_g}{A_{pm} l_g} H_m \quad (8)$$

That represents a straight line with a negative slope (shown in Figure 4) called a working line. It is a function of the geometrical characteristics of the magnetic circuit. The location of the operating point P_1 is at the intersection of the demagnetization curve with the straight line given by Eq (8).

By changing the geometrical characteristics, the operating point is modified (see P_2 in Figure 4). In particular, the second point results below the knee. Therefore, this configuration yields an irreversible demagnetization of the PM.

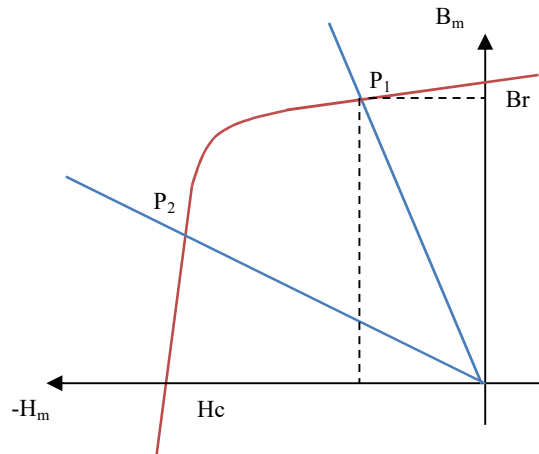


Figure 4 PM operating point

Effect of external magnetic field intensity

In this case, an external demagnetizing current linkage is introduced in the permanent magnet circuit, as shown in Figure 5.

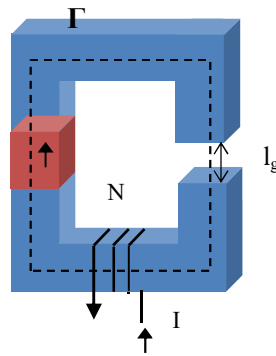


Figure 5 Magnetic circuit with current

A contribution of the external source is presented in the *Ampere's law* (9):

$$\oint_{\Gamma} \vec{H} \cdot d\vec{l} = H_{pm} l_{pm} + H_g l_g = -NI \quad (9)$$

Where N is the number of coil turns. Regarding the *Gauss's law*, it remains the same of the previous case. The magnetic flux density of the PM is given by Eq. (10):

$$B_{pm} = -\mu_0(H_{pm}l_{pm} + NI) \frac{A_g}{(l_g A_{pm})} \quad (10)$$

The overall effect is a shift of the previous working line, at higher values of the intensity field (green line in Figure 6). This effect is given by the demagnetization current.

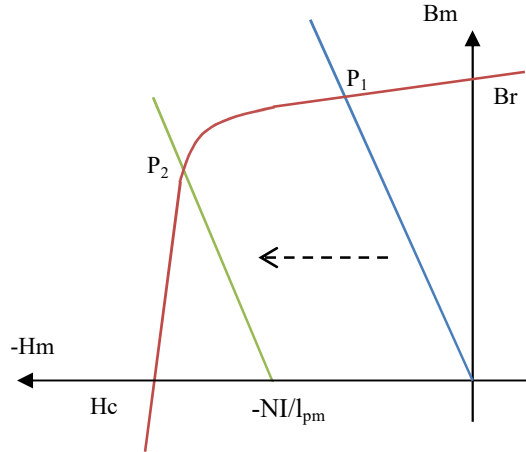


Figure 6 Operating point with armature current

In that situation, the external magnetic field tends to demagnetize the PM. As consequences, the current influences the selection of the PM operating point. The selection of the PM's characteristics (material and size) is usually evaluated respecting on the maximum external current, namely in the short circuit state.

Dependence of Temperature

A characteristic thermal parameter for the PMs is the so called *Curie temperature* (T_c).

Above such value, the material loses its magnetism. However, considerable performance deterioration is already detected well below the Curie temperature.

Below the Curie temperature, the domains are aligned in the absence of an applied magnetic field (Figure 7). In this case, the material is called *ferromagnetic*. Above T_c , the magnetic domains are randomly aligned unless the magnetic field is applied. The material above T_c is called *paramagnetic* (Figure 8). The characteristic parameter is given by the susceptibility (χ_m) defined by the second Curie's law in (11):

$$\chi_m = \frac{C_c \rho}{T - T_c} \quad (11)$$

It is functioning of material-specific Curie constant (C_c) and the material density (ρ).

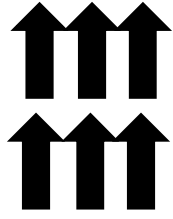


Figure 7 Ferromagnetic below T_c

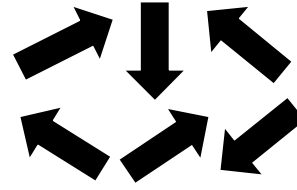


Figure 8 Paramagnetic above T_c

The maximum operating temperature (T_{max}) is the temperature above which the performance starts to decrease.

The parameters B_r and H_c are depending on the temperature by Eq (12):

$$\begin{cases} B_r(T) = B_{r0} \left(1 + \frac{k_{Br}(T - T_0)}{100} \right) \\ H_c(T) = H_{c0} \left(1 + \frac{k_{Hc}(T - T_0)}{100} \right) \end{cases} \quad (12)$$

Where T_0 is the initial temperature and k_{Br} , k_{Hc} are the temperature coefficients which depend on the magnet properties and they are usually given by the manufacturer. Figure 9 shows the behaviour of magnetic field and flux density with the variation of the temperature. As illustrated, the performance (indicated by the *Maximum energy product*) is decreasing for higher temperatures. Moreover, high temperatures increase the risk of demagnetization.

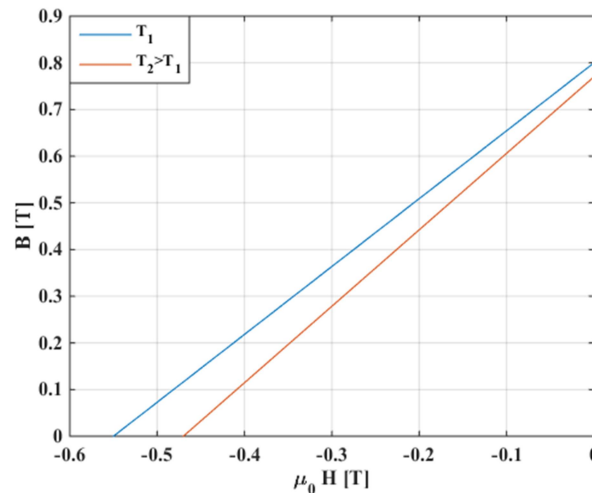


Figure 9 B-H curves depending on temperature

The main PMs currently used for electric motors are:

- Ferrites
- Rare Earth materials (Samarium Cobalt $SmCo$ and Neodymium Iron Boron $NdFeB$)

Ferrites were developed in the 1950s. They are characterized by the low price and high Curie temperature. Moreover, they have a very high electrical resistivity, which represents a clear advantage for decreasing the eddy current losses. Therefore, these compounds are still implemented for small motors, generators and sensors.

Rare earth materials were invented in the 1960s, they are used for high energy solutions, such as motors for hybrid vehicles.

Samarium-Cobalt (SmCo) has a good compromise between operating temperature and maximum energy product. These magnets have a linear behaviour. However, the high cost is one of their drawbacks.

For the highest energy performances, *Neodymium Iron Boron* is the most suitable permanent magnet. A summarize of principal characteristic is listed in Table 1.

	B_r (T)	H_c (kA/m)	BH_{max} (kJ/m ³)	T_c (°C)	T_{max} (°C)	Density kg/m ³
Ferrite	0.38	250	35	450	300	4800
SmCo	0.85	570	100	775	250	8300
NdFeB	1.15	880	240	310	180	7450

Table 1 Main propriety of hard magnetic materials [2]

Figure 10 shows the intrinsic curves for the mentioned magnets. It is possible to evaluate the different maximum energy product ($B-H_{MAX}$). Applications with rare earth materials allow to have the smallest PM volume with the same flux and the same demagnetization limit however, they are expensive. Machines with Ferrite need of *PM* larger sizes to achieve the same performances of the rare earth materials, whereas the magnetic flux density is below 0.4T.

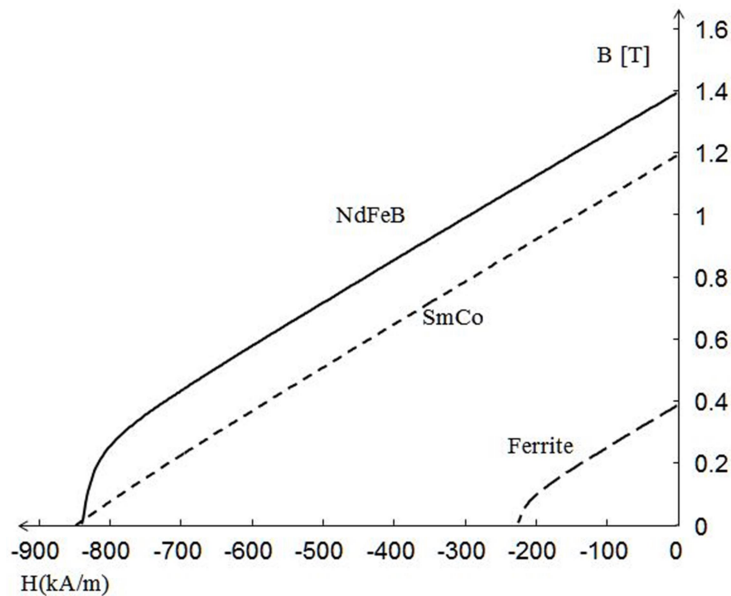


Figure 10 B-H normal curves of different PMs

Neodymium Iron Boron

Neodymium Iron Boron (*NdFeB*) is the most widely used type of rare earth magnet in the PMSM. It is the strongest type of permanent magnet. The particular crystal structure of this material gives to the compound the potential to have a high coercive field and therefore high power density.

Curie temperature of *NdFeB* is about 310°C, but already at 250°C the value of coercive field strength is zero. A partial substitution of the Neodymium (N_d) with another rare earth material such as Dysprosium D_y , increase the value of H_c . In this way, it is possible to increase the maximum operating temperature.

Neodymium magnets are classified in grades that measure the strength of magnet, the first letter is always *N* that means Neodymium, followed there are two digit numbers that represent the maximum energy product (unit of measurement Mega Gauss-Oersted) and in the end, the last letter(s) represent the maximum operating temperature, as showed in the Table 2.

Letter	M	H	SH	UH	EH	VH
Maximum operating Temperature (°C)	100	120	150	180	200	230

Table 2 Maximum operating temperature *NdFeB*

Figure 11, for instance, shows the demagnetization curves (intrinsic and normal) of the material *N33H* from *Arnold Magnetic Technologies*. It shows the impact of the temperature and how these curves decrease slowly initially with the increase in $-H$ and then drop off quickly when the knees are passed. With the same working line (*green-line*) at 150°C curve, the knee occurs rapidly, therefore the risk of demagnetization increases. Magnet temperature increases substantially when the motor is overloaded.

1.2 PMSM

Permanent Magnet Synchronous Machines (PMSM) are widely used in electric vehicles. The advantages of these machines are:

- High power density and high efficiency
- Absence of rotor windings
- Low inertia
- High torque at low speed

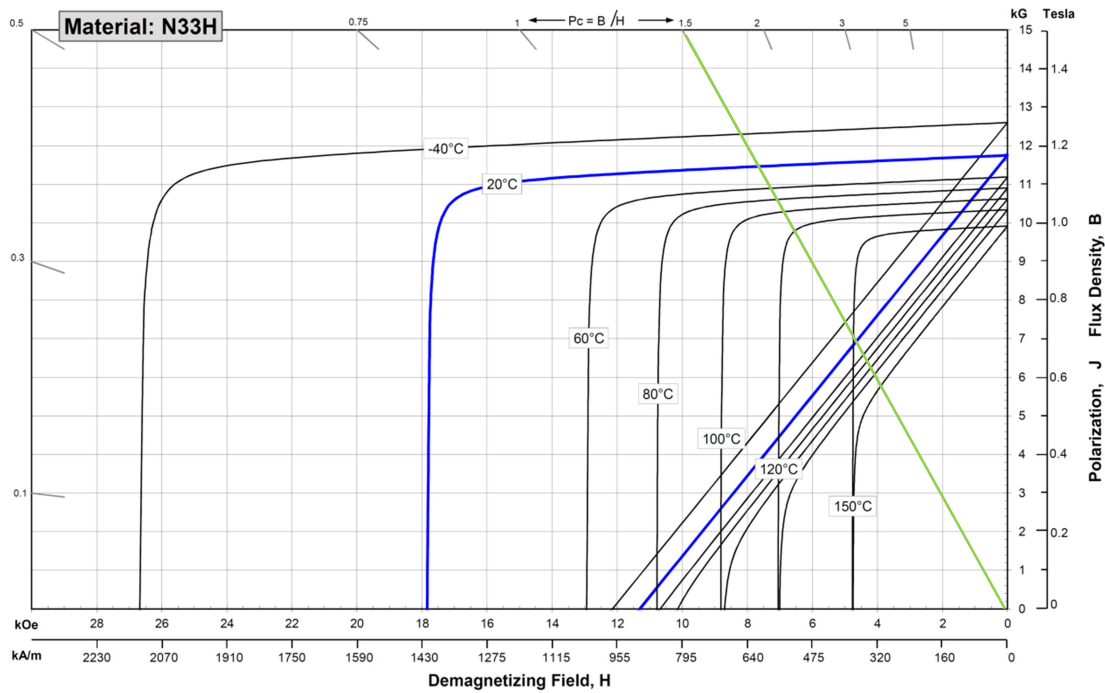


Figure 11 Impact of temperature on N33H (Source: Arnold Magnetics)

The basic components are the rotor with permanent magnets and the stator containing the windings. The rotating magnetic field of the stator is provided by their currents while that of the rotor comes from the permanent magnets.

They are called synchronous machine because they operate at synchronous speed (Ω), namely the speed at which the magnetic field rotates. This speed is a function of power supply frequency (f) and by the number of pole pairs (p) in the machine:

$$\Omega = p\omega = p(2\pi f) \quad (13)$$

Where the Ω and ω are electrical and mechanical angular speed respectively. It is also often expressed as number of revolution minute n :

$$n = 60 \frac{f}{p} \quad (14)$$

Furthermore, these machines are classified by the wave shape of the back electromotive force (*trapezoidal* and *sinusoidal*) or by the field flux direction (*axial* and *radial*). Regarding the PMs placement, the PMSM can be classified as:

- IPMSM Interior Permanent Magnet Synchronous Machines (Figure 12a)
- SPMSM Surface Permanent Magnet Synchronous Machines (Figure 12b)

Figure 12a shows an IPMSM. In this case, the magnets are inserted into specific slots. The white surfaces are composed of air.

Figure 12b shows a SPMSM with the magnets mounted on the outer rotor circumference.



Figure 12 Different configurations of PMSM

1.3 Mathematical Model

During the thesis, a mathematical model for the PMSM is derived for only radial flux machines. A three-phase machine can be generally modelled as shown in Figure 13a. It is assuming a stator winding connected in star configuration and arranged in three coils and for simplicity the rotor has a single pole pair ($p=1$).

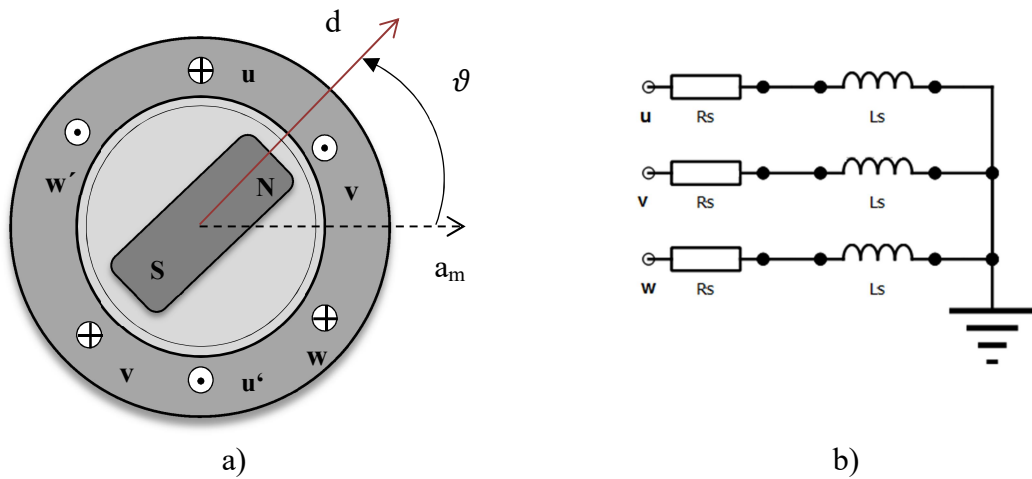


Figure 13 A simplified representation of a three-phase PMSM

Neglecting the iron loss and the leakage flux and assuming a sinusoidal air-gap flux density the voltage equations based on the stator equations (*phase coordinate*) can be written as Eq (15):

$$\begin{bmatrix} U_u \\ U_v \\ U_w \end{bmatrix} = \begin{bmatrix} R_s & 0 & 0 \\ 0 & R_s & 0 \\ 0 & 0 & R_s \end{bmatrix} \cdot \begin{bmatrix} I_u \\ I_v \\ I_w \end{bmatrix} + \frac{d}{dt} \begin{bmatrix} \Psi_u \\ \Psi_v \\ \Psi_w \end{bmatrix} \quad (15)$$

Where R_s is the stator resistance, I is the current through the coil and Ψ is the linked flux in each phase. The flux-current relation in phase-coordinate is given by Eq. (16):

$$\begin{bmatrix} \Psi_u \\ \Psi_v \\ \Psi_w \end{bmatrix} = \begin{bmatrix} L_{uu} & M_{uv} & M_{uw} \\ M_{vu} & L_{vv} & M_{vw} \\ M_{wu} & M_{wv} & L_{ww} \end{bmatrix} \cdot \begin{bmatrix} I_u \\ I_v \\ I_w \end{bmatrix} + \begin{bmatrix} \Psi_{PMu} \\ \Psi_{PMv} \\ \Psi_{PMw} \end{bmatrix} \quad (16)$$

Where L_{uu} , L_{vv} , L_{ww} are the self-inductance of the stator windings, M_{uv} , M_{vu} , M_{vw} are the mutual inductances of the stator windings and Ψ_{PMu} , Ψ_{PMv} , Ψ_{PMw} Are the PM flux linkage. The self-inductance and the mutual inductance are calculated by [3] :

$$\begin{aligned} L_{uu} &= L_{ls} + L_A + L_B \cos(2\vartheta) \\ L_{vv} &= L_{ls} + L_A + L_B \cos\left(2\vartheta - \frac{2\pi}{3}\right) \\ L_{ww} &= L_{ls} + L_A + L_B \cos\left(2\vartheta - \frac{4\pi}{3}\right) \\ M_{uv} &= M_{vu} = -\frac{1}{2}L_A + L_B \cos\left(2\vartheta - \frac{2\pi}{3}\right) \\ M_{uw} &= M_{wu} = -\frac{1}{2}L_A + L_B \cos\left(2\vartheta - \frac{4\pi}{3}\right) \\ M_{vw} &= M_{wv} = -\frac{1}{2}L_A + L_B \cos(2\vartheta) \end{aligned}$$

Where L_{ls} is the *leakage* inductance of the stator winding, L_A and L_B are the inductance parameter and ϑ namely, the electrical angle between the PM magnetic axis (*d-axis*) and the magnetic axis of u-phase (a_m) as shown in Figure 13a and it can be written as:

$$\vartheta(t) = \int_0^t \omega(\tau) d\tau + \vartheta(0) \quad (17)$$

The PM fluxes linking the stator windings are given by Eq (18):

$$\begin{cases} \Psi_{PMu} = \Psi_{PM} \cos(\vartheta) \\ \Psi_{PMv} = \Psi_{PM} \cos\left(\vartheta - \frac{2\pi}{3}\right) \\ \Psi_{PMw} = \Psi_{PM} \cos\left(\vartheta - \frac{4\pi}{3}\right) \end{cases} \quad (18)$$

In conclusion, in the phase coordinates the equations are non-linear differential and with time-varying coefficients, namely the self and mutual inductances. Furthermore, the equation set listed above can be written is a more compact form:

$$\begin{cases} [U] = [R][I] + \frac{d}{dt} [\Psi] \\ [\Psi] = [L][I] + [\Psi_{PM}] \end{cases} \quad (19)$$

The d-q coordinate model

It is possible to move from the 3-phase reference system to a new one (*d-q*) where the equations are always non-linear but the coefficients are position independent.

The $d-q$ reference system is orthogonal and it is fixed on the rotor. This transformation was developed first by *Clarke* and then from *Park*. The Clarke transformation moves from a three-phase reference system to an orthogonal stationary reference frame α - β fixed on the stator as shown in Figure 14. In this case, it is chosen that the α -axis is aligned with the magnetic axis of u-phase.

Clarke matrix C is used for the transformation¹ and it is given by:

$$\begin{pmatrix} I_\alpha \\ I_\beta \end{pmatrix} = C \begin{pmatrix} I_u \\ I_v \\ I_w \end{pmatrix} = \frac{2}{3} \begin{bmatrix} 1 & -1/2 & -1/2 \\ 0 & \sqrt{3}/2 & -\sqrt{3}/2 \end{bmatrix} \begin{pmatrix} I_u \\ I_v \\ I_w \end{pmatrix} \quad (20)$$

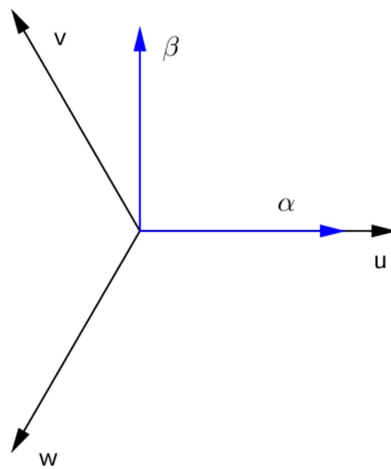


Figure 14 Clarke Transformation

Even in the Clarke reference system the coefficients are a function of the rotor angle. To delete this dependence *Park* invented a new rotating reference frame ($d-q$) locked on the rotor, as shown in Figure 15. Therefore, by using the Park transformation the inductances became independent of the rotor position. The $d-q$ reference system revolves at the electrical rotational speed (ω). To move from the in α - β coordinate to $d-q$ coordinate a rotation matrix R (21) is used.

$$\begin{pmatrix} I_d \\ I_q \end{pmatrix} = R \begin{pmatrix} I_\alpha \\ I_\beta \end{pmatrix} = \begin{bmatrix} \cos(\theta) & \sin(\theta) \\ -\sin(\theta) & \cos(\theta) \end{bmatrix} \begin{pmatrix} I_\alpha \\ I_\beta \end{pmatrix} \quad (21)$$

¹ The homopolar component is zero with the assumption of symmetrical and balanced system.

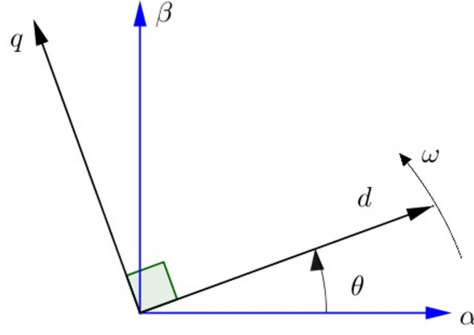


Figure 15 Park Transformation

The Park matrix can be expressed as the product of Clarke matrix and the rotational matrix:

$$[P(\theta)] = [R(\theta)][C] = \frac{2}{3} \begin{bmatrix} \cos(\theta) & \sin(\theta) \\ -\sin(\theta) & \cos(\theta) \end{bmatrix} \begin{bmatrix} 1 & -1/2 & -1/2 \\ 0 & \sqrt{3}/2 & -\sqrt{3}/2 \end{bmatrix} \quad (22)$$

The overall relations between the two reference systems are:

$$U_{dq} = [P(\theta)]U_{uvw}; \quad I_{dq} = [P(\theta)]I_{uvw}; \quad \Psi_{dq} = [P(\theta)]\Psi_{uvw}$$

To move from the u-v-w reference system to d - q one, the angular position of the rotor ϑ is needed.

In accordance with [3], the d - q reference system equations are expressed as:

$$\begin{cases} U_d = R_s I_d + \frac{d\Psi_d}{dt} - \omega \psi_q \\ U_q = R_s I_q + \frac{d\Psi_q}{dt} + \omega \psi_d \end{cases} \quad (23)$$

$$\begin{cases} \psi_d = L_d I_d + \psi_{PM} \\ \psi_q = L_q I_q \end{cases} \quad (24)$$

Defined α the stator current phase angle from the q -axis, the current equation can be written as:

$$\begin{cases} I_d = I_s \sin(\alpha) \\ I_q = I_s \cos(\alpha) \end{cases} \quad (25)$$

Figure 16 shows the phasor diagram of a PMSM, with the reference angle. The angle β is the current phase angle.

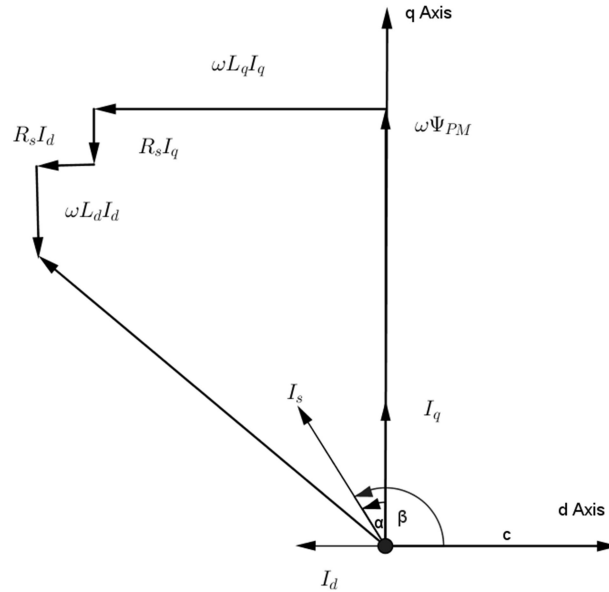


Figure 16 Phasor Diagram PMSM

From the power balance and the mechanical power, the torque can be expressed as a function of the d-q currents (26):

$$T_e = \frac{3}{2}p\psi_{PM}I_q + \frac{3}{2}p(L_d - L_q)I_dI_q \quad (26)$$

The formula is valid even with $p \neq 1$.

The first term of Eq.(26) is called *permanent magnet torque* and the second one *reluctance torque*. The second term depends on the values of the direct and the quadrature inductances, as described in the following subchapter.

From Figure 16 the torque can be written in function of the stator current and of his phase angle as:

$$T_e = \frac{3}{2}p\psi_{PM}I_s \sin(\beta) + \frac{L_d - L_q}{2} I_s^2 \sin(\beta) \quad (27)$$

In this way, it is possible to plot the two torque components in function of the current-phase angle, as shown in Figure 17.

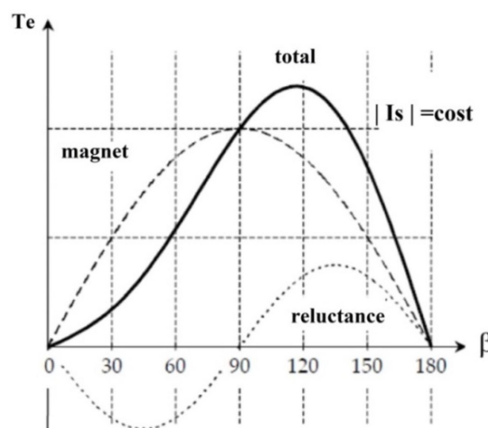


Figure 17 Magnet-Reluctance Torque

1.3.1 Direct and Quadrature Axis Inductances

The inductances in an electric machine can be evaluated by dividing the value of the magnetic flux linkage by the current:

$$L = \frac{\Psi}{I} \quad (28)$$

In the d - q reference system and for a PMSM the flux is divided along the direct and quadrature direction and therefore the inductances are given by Eq (29):

$$\begin{cases} L_q = \frac{\psi_{sq}}{I_q} \\ L_d = \frac{\psi_{sd} - \psi_{PM}}{I_d} \end{cases} \quad (29)$$

From the *Hopkinson's* law, the magnetic flux linkage is expressed as Eq. (30):

$$\Psi = \frac{mmf}{\mathcal{R}} = \frac{NI}{\mathcal{R}} \quad (30)$$

Where N is the turns number and \mathcal{R} is the magnetic reluctance which depends on the geometrical and material characteristics of the magnetic circuit and it is defined as Eq. (31):

$$\mathcal{R} = \frac{l}{\mu_0 \mu_r S} \quad (31)$$

Therefore, the magnetic reluctance assumes an important role for computing the inductance values. These inductances can be different depending on iron rotor structure that is directly connected to the magnet placement.

Practical configurations of the PM are shown in Figure 18. Since the PM 's relative permeability is near to the unit, for evaluating the magnetic reluctance the magnets must be considered as air ($\mu_{r_{PM}} \approx \mu_{r_{air}} \approx 1$).

Figure 18a represents a classic arrangement of *Surface Mounted* PMSM [4]. The flux path along the direct and the quadrature axis is the same due to the uniform distribution of the magnets. Therefore, the values of the inductances along the two orthogonal axes are equal (or nearly equal). In the SPMSM, the reluctance torque disappears.

In Figure 18b is shown an IPMSM, in this case the flux path is different. In the quadrature axis is present more iron than the direct one. Therefore, the reluctances and then the inductances are different. In conclusion, for an IPMSM are present both terms of Eq. (26).



Figure 18 a) SPSM Isotropic b) IPMSM Anisotropic [4]

1.4 Scientific Contribution

Alberti & Bianchi [5] have studied the fractional slots windings. By using the *star of slots*, the balanced and symmetrical winding design is achieved. The results of this work show as this configuration allows to reduce the end-winding losses and the torque ripple.

Finker & Hameyer [6] have calculated the losses depending on different values of current, field-weakening angle and rotational speed of an IPM motor. The results show that the field-weakening angle should be controlled to reduce the rotor losses. In order to move the losses from the rotor into the stator, the field-weakening angle can be decreased. In this way, the magnets are protected from the heat. Moreover, it is possible to dissipate more easily the heat presented in the stator by means of a water-cooling jacket. The authors have studied the effect of the harmonics on the losses for several current shapes.

Pyrhönen, Jokinen, Hra [7] have studied the winding connection for fractional slots and the effect of the removing of certain harmonics. Furthermore, a method to find the symmetrical and balanced winding connection has been developed.

Doppelbauer [8] has studied the procedure to calculate the efficiency map. Furthermore, an interpolation formula to determine the losses with seven points has been studied.

Mellor, Roberts and Turner [9] have calculated the lumped parameter thermal network for a total enclosed fan-cooled (TEFC) electric motor. This paper is the base of the thermal studies.

2 Motor Characteristics and Sizing

The motor is installed on an electric scooter drawn for the urban city and developed to decrease the energy cost and the CO₂ emission. In the electric vehicles, there is not much space aboard and the batteries often occupy the most of it. Therefore, the propulsion power is delivered by small motors designed to achieve high efficiency within a large range of the torque-speed characteristic, high power/weight ratio and high reliability. In the case under study, such requests are obtained by using a Surface PMSM, its main characteristics are listed in Table 3.

Typology	Surface Mounted PMSM
Position Sensor	Resolver 6 poles
Number of pole pairs (p)	6
Number of phases (m)	3
Cooling	Water
Insulation class	F (155 °C)

Table 3 Motor Characteristics (Internal Source)

In Table 4 are listed the mechanical and electrical characteristic given by the manufacturer.

DC bus voltage	U_{DC}	125 V
Maximum power	P_{MAX}	35269 W
Maximum torque	M_{MAX}	74.6 Nm
Maximum current	I_{MAX}	500 A
Continuous stall torque	M_0	46.6 Nm
Continuous stall current	I_0	279.8 A
Idle speed	n_0	6789 rpm
Rated power	P_n	33387 W
Rated torque	M_n	35.82 Nm
Rated current	I_n	207.1 A
Rated speed	n_n	8900 rpm
Base speed	n_b	4500 rpm

Table 4 Motor characteristics (Internal source)

Figure 19 shows the characteristic of the torque (black line) and of the mechanical power (orange line) regarding the speed. $M_{s/l}$ and $P_{s/l}$ are the motor characteristics when it works for

enough time without exceeding the maximum temperature. M_{max} and P_{max} are the characteristics when the motor is fed with the maximal current. M_{max} is applied only for a short time to avoid the risk of thermal overloaded.

Regarding the speed, it is possible to identify a characteristic point: the base speed. It is the speed where the machine achieves the maximum voltage value of the inverter. Since the stator flux is given by the ratio of the stator voltage to the power supply frequency, the fact that the voltage is constant implies that beyond this point, in order to increase the mechanical speed, flux weakening must be employed. Therefore, even the torque value decreases.

The base speed divides the torque-speed graph in two parts:

- Constant Torque region $n < n_{base}$
- Flux Weakening region $n > n_{base}$

In the constant torque region, the power increases from zero to the rated power, beyond the base speed the power remains constant.

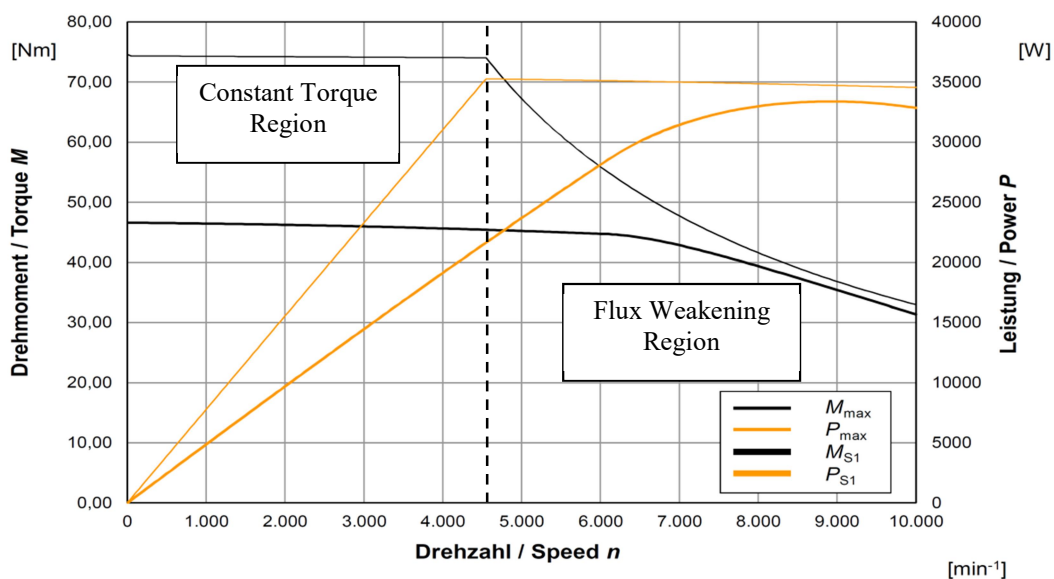


Figure 19 Torque-Speed curve of the motor (Internal source)

2.1 Motor Design

Figure 20 shows the motor components. The external frame is made with aluminium and the principal purpose is to give mechanical support for the machine. Furthermore, it is composed of the cooling jacket, within which circulates an external fluid for decreasing the inner temperatures.

The electromagnetic part is placed inside the frame and it is composed of the following elements:

- Stator core
- Windings
- Rotor core
- Permanent magnets

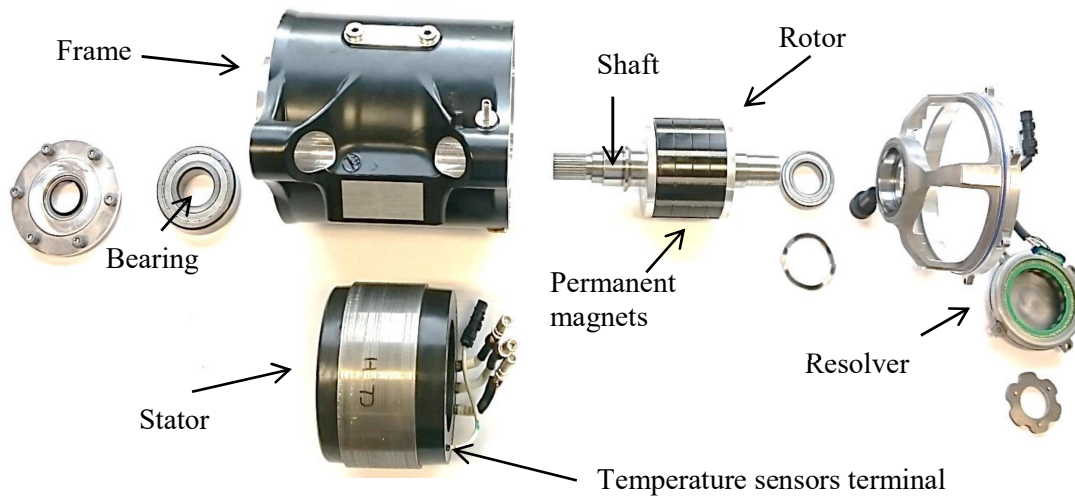


Figure 20 Explosion of the motor components

The stator and rotor cores are composed of insulated laminations steel, which are stacked to make the active length (L). The material chose for this analysis is the *NO20* since the real lamination presents the same thickness. *Cogent Power* realizes it for automotive applications, since the main advantages are the lightness and good thermal conductivity. In addition, the thickness value is chosen to minimize the eddy current losses.

The rotor core is punched to reduce the overall weight. The magnets are installed on the rotor surface. Such that components present a cylindrical structure segmented both on the axial and circumferential direction for reducing the eddy current losses and risk of damage. The magnets present a multipole radial magnetization as shown in Figure 21.

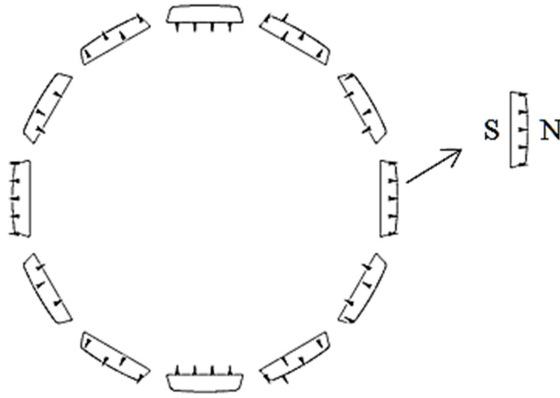


Figure 21 PM radial magnetization

Since the distribution of magnetic fields inside the stator is not uniform, it is divided into two parts: *teeth* and *yoke*. In fact, the teeth are the stator part near to the region where most of the energy is stored (*air-gap*).

The stator is constituted by the semi-closed slots where the windings are arranged. The design of the stator winding is studied in the next subchapter.

The isometric view of the motor is shown in Figure 22. In particular, it is drawn only the active length. The 3D CAD model is created with the *JMag Designer Geometry Editor*, where:

- Frame (light blue)
- Stator yoke (orange)
- Stator teeth (green)
- Windings (yellow)
- Permanent magnets (blue)
- Rotor (grey)
- Shaft (red)

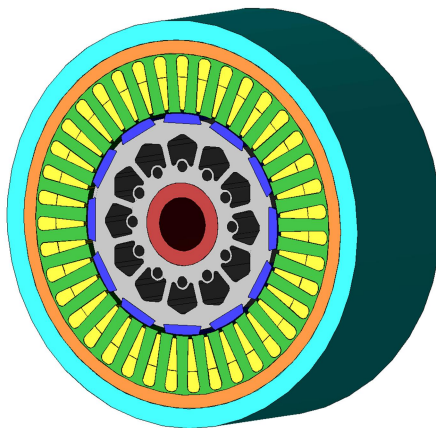


Figure 22 Motor CAD

2.2 Winding

Windings are placed within the stator slots, which are semi-closed topology and equally spaced along the stator inner periphery.

In detail, the slot is composed of copper, conductor insulation and slot insulation, as shown in Figure 25. Regarding the insulation, an index called the *insulation class* is defined, which represents the maximum allowable operation temperature. Beyond this value, the insulation life decreases rapidly until the failure. For this reason, the thermocouples are installed for monitoring the temperature. However, the motors are designed for operating at an average temperature below the maximum allowable value.

The coil is divided in two parts: the *coil side* that represents the part of coil located in the slot and the *coil end* that is the part of the coil outside the slot. Both coil ends constitute the end windings, as shown in Figure 23.

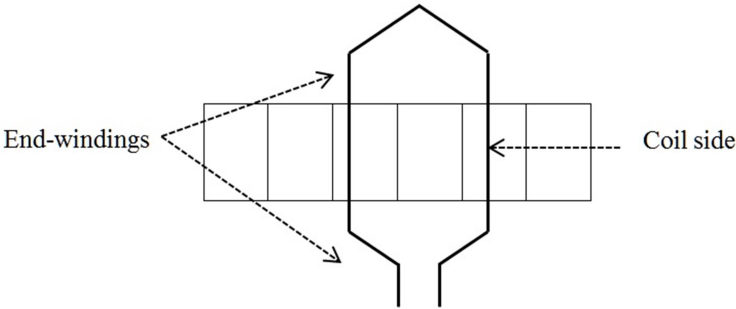


Figure 23 Coil

In each slot, one (*single-layer*) or more coils (*multi-layers*) can be placed. In this study, the machine presents a distributed winding with double-layer configuration (*top* and *bottom*) as shown in Figure 24.

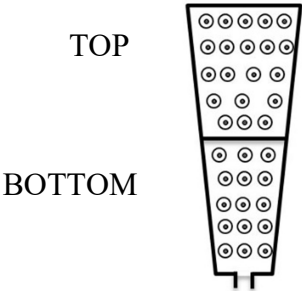


Figure 24 Double-layer windings

Slot Fill Factor

The slot fill factor is defined as the ratio between the parts of the area occupied by the copper on the total area of the slot. Figure 25 shows a simplified cross section of stator slot.

In order to evaluate this index, the wire size and the *number of conductors per slot* are needed. The wire diameter was measured through a caliper and matched with the wires available on the market. The *number of conductors per slot* is an integer and for a double layer winding it must be a multiple of two. The characteristics of the chosen wire are listed in Table 5.

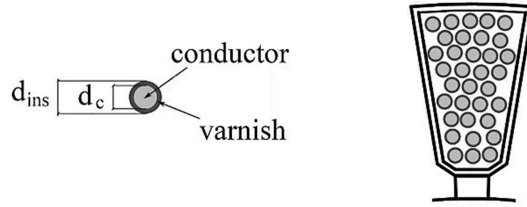


Figure 25 Slot fill factor

Parameter	Symbol	Value
Copper Diameter	d_c	0.5 mm
Copper Area	S_c	0.196 mm ²
Diameter with insulant	d_{ins}	0.587 mm
Insulant thickness		0.044 mm

Table 5 Wire parameter

By using the geometry tool of the Cad Software, the whole slot area was computed.

Parameter	Symbol	Value
Slot Area	S_{slot}	80 mm ²
Number of wires per slots	Nt	164
Copper Area	S_c	32.2 mm ²

Table 6 Slot geometry

$$Slot\ Fill\ Factor = \frac{S_c}{S_{slot}} = 36\% \quad (32)$$

2.2.1 Stator Winding Design

The aim of this chapter is to design one of the possible balanced and symmetrical three-phase windings. A winding is balanced and symmetrical if the coils arrangement is able to produce a symmetrical system of three *emfs* all of the same magnitude, waveform and displaced by 120°.

The motor has the number of stator slots (Q) equal to 39, pole pairs number (p) equal to 6 and the number of phases (m) equal to 3. Therefore, the number of slots per pole and phase q is given by Eq.(33):

$$q = \frac{Q}{2mp} = \frac{39}{2 \cdot 3 \cdot 6} = \frac{13}{12} = \frac{n}{z} \quad (33)$$

Since this number is not an integer and superior to the unit, the design is called *fractional-slot* winding. It is used in the many applications that need high torque at low speed, for reducing the torque ripple and to minimize the end-winding lengths.

The following analysis refers to the top layer, whereas the bottom layer is obtained by using the coil-span, as explained later.

In order to design the balanced and symmetrical winding, a *star of slots* is needed. It is a graphic representation of the phasors of *electromotive force* induced in each coil side.

Considering a sinusoidal distribution of the B in the air-gap, for the Faraday-Lenz law the emf can be expressed by Eq.(34):

$$e = BLv \quad (34)$$

Where B is the air-gap flux density, L is the active length, v the rotor rotational speed.

Since the winding is distributed, the B does not intersect all coil sides simultaneously, the induced *emf* in each coil side has a certain phase shift.

In every electrical machine, there is a periodicity or rotational symmetries of the *emf*. It is determined as the greater common divisor between the number pole pairs p and the slots number Q .

$$t = G.C.D.(Q, p) \quad (35)$$

It means that there are t identical star of slots. Exploiting the rotational symmetry, a reduced voltage phasor diagram can be studied. It is composed by a Q/t number of spokes out of phase by an angle α_z given by Eq. (36):

$$\alpha_z = \frac{360}{Q} t \quad (36)$$

The angle between the emf phasors of two adjacent slots α is given by Eq.(37):

$$\alpha = \frac{p}{t} \alpha_z \quad (37)$$

For the PMSM under analysis, the parameters are listed in Table 7.

Parameter	Symbol	Value
Number of slots	Q	39
Number of pole pairs	p	6
Number of phases	m	3
Number of stars	t	3
Number of spokes	Q/t	13
Phasor skipped		1
Angle between of adjacent spokes	α	27.69
Slot angle	α_z	55.8

Table 7 Star of slots parameter

When the phasor skipped is equal to one, it means that between two consecutive phasors (divided by an angle of α_z) an additional phasor is collocated.

Figure 26 shows the voltage phasor diagram with 3 concentric stars. Each phasor is numbered according to the number of the slot that contains the corresponding induced emf.

Each star is divided into six sectors (positive and negative). For each phase, two opposite sectors are assigned. In the positive sector, the induced emf in the coil side assumes a positive value while in the opposite sector it assumes a negative value.

Figure 27 show the sectors of the first star of slots. The full area represents the positive sectors, whereas the dotted area represents the negative sector.

Since the number of spokes for each star is equal to 13, it does not allow an equal number of phasors in the positive and negative sectors. The spokes number per phase and star are listed in Table 8.

T	U	V	W
1	5	4	4
2	4	5	4
3	4	4	5

Table 8 spokes number configuration

For each star, one phase has five phasor while the others only four, as shown in Figure 27, where the symbols $\oplus \ominus$ represent respectively the positive and negative voltage phasor.

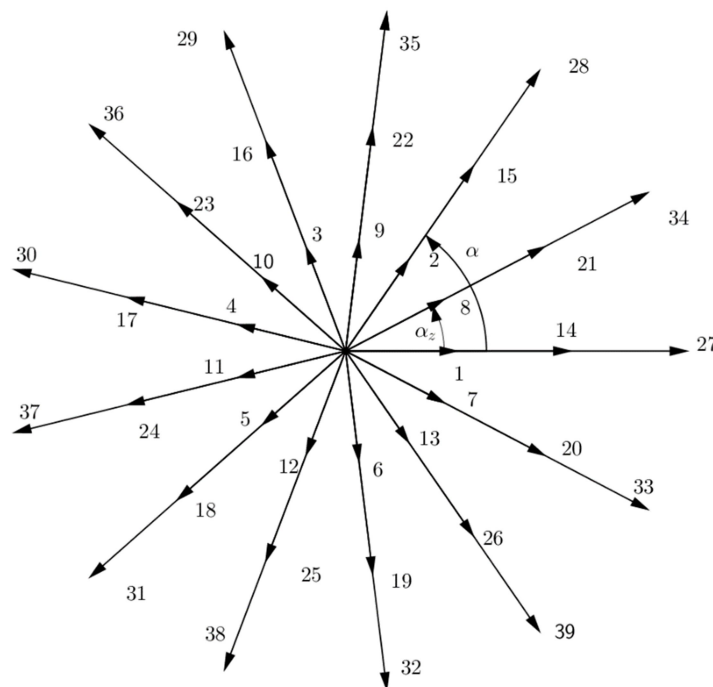


Figure 26 Voltage phasor diagram

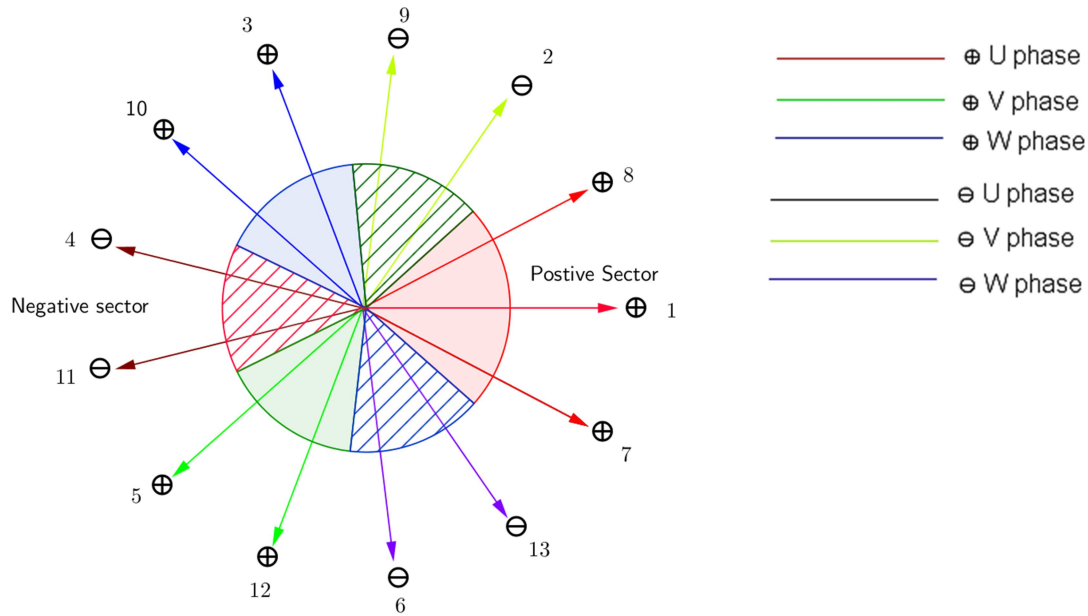


Figure 27 Sector of star of slots

In order to obtain the bottom layer, the coil span is needed. Such parameter is the distance between one conductor and the corresponding return conductor². Starting from this information, it is possible to achieve the bottom layer design by shifting the *coil span* and reversing the coil sides polarity of the top layer configuration. The coil span was first evaluated analytically and then it was tested in an experimental way. The analytic equation is shown in Eq (38).

$$y = \frac{Q}{2p} = \frac{39}{12} = 3.25 \quad (38)$$

Two options are possible, since 3.25 is closer to 4 and 3. With a coil-span of 3 slots the end-winding length is minimized and therefore, a copper saving.

In the experimental way, the motor was cut in two parts. By using the multimeter set in *Continuity Test Mode*, the connection between each slot was tested. The result is a coil span of 3 slots, as expected. Figure 28 shows the coil span.

² <http://www.emotor.org/glossary/coil-span/>

Table 11 shows the algebraic sum of this configuration. The magnitudes of the three overall emfs are about 123 V. The U-W offset angle is equal to 119.35° and U-V offset angle is equal to -119.35°. This proves that the winding design is symmetrical and balanced.

		Real (V)	Im (V)	Magnitude (V)	Phase (°)
TOP	U	123.675	0.000	123.675	0
	V	-60.195	-107.062	122.824	-119.35
	W	-60.195	107.062	122.824	119.35
BOTTOM	U	120.081	-29.597	123.675	-13.85
	V	-84.068	-89.545	122.824	-133.19
	W	-32.825	118.357	122.824	105.50

Table 11 Algebraic sum of phasor for top and bottom layer

Figure 29 shows the voltage phasor diagram, which proves that the winding is symmetrical and balanced. Where with the letter E is represented the emf in the coil side and the number the relative slot. The sign of each emf is in accordance with Table 10.

A parameter that characterises winding is the distribution factor and it is expressed as a ratio of the phasor sum of the emfs induced in all the coils distributed in a number of slots under one pole to the arithmetic sum of the emfs induced.

$$k_d = \frac{emf_T}{\sum_{i=1}^{13} em_i} = 0.94$$

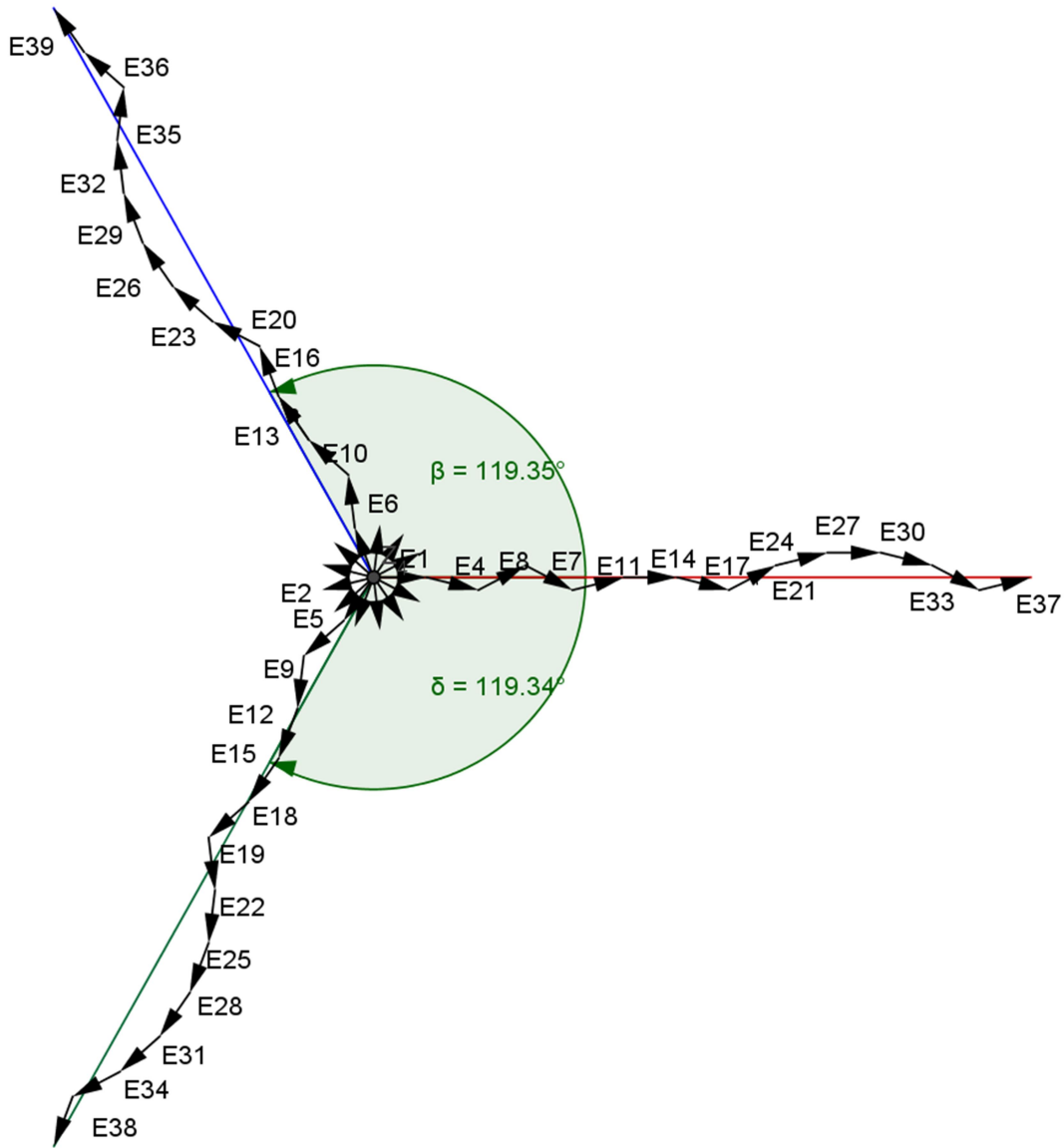


Figure 29 Phasor diagram

2.3 Winding Stator Resistance

A multimeter was utilized to measure the winding stator resistance. Since the expected value is low, a four-terminal configuration of the multimeter is preferred. Such configuration allows the measurement of low impedances in a more accurate way, reducing the effect of lead resistance. Figure 30 exhibits the four terminal configurations. R_s' is the stator winding resistance.

A couple of leads (HI, LO) are used to inject test current (I_{tar}) through the R_s' . To avoid the voltage drops on the resistances R_p , the voltage is measured through the other leads (*Sense leads*).

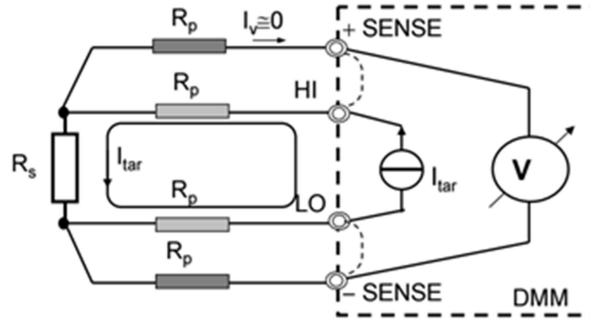


Figure 30 Four-terminal sensing

Since the multimeter has infinite resistance, the current I_v that flows through the *sense* leads, can be neglected. Therefore, even the voltage drops across the leads resistances. Consequently the voltage measured (V_s) with the multimeter correspond to the voltage on the R_s' .

$$R_s' = \frac{V_s}{I_{tar}} \quad (39)$$

However, the stator windings have a star connection, therefore, the measure from the multimeter must be divided by 2.

$$R_s = \frac{R_s'}{2} = \frac{0.0083}{2} = 0.00415 \, \Omega \quad (40)$$

Where R_s' is the phase-phase resistance.

2.4 Losses

In order to calculate the distribution of heat inside the electrical machine, a power loss analysis is required. The losses represent the heat source and they are given by the following elements:

- Resistive losses
- Iron losses
- Permanent magnet losses
- Mechanical losses

Resistive Losses

Resistive losses occur in the conductors and they are often called *Joule* or *Copper* losses. They depend on the current value and on the winding resistance. Furthermore, they are also influenced by the temperature rise.

$$P_j = 3 R_s I_{RMS}^2 \quad (41)$$

Iron Losses

The iron losses are the second major thermal source in the electric machines. These losses are due to the time variation of the magnetic flux density B . Moreover, they are divided into hysteresis loss and eddy current loss.

The iron parts in the machines are the stator and the rotor. The stator, in turn, can be divided in stator yoke and stator teeth. In these two parts, the flux density is different and for this reason, their losses are calculated separately as shown in Eq. (42):

$$P_{Fe} = (p_{h-t} + p_{ec-t})M_t + (p_{h-y} + p_{ec-y})M_y \quad (42)$$

Where the subscripts h , ec , t , and y represent hysteresis, eddy current, teeth and yoke respectively, M is the mass and p is the specific loss.

Specific Hysteresis Loss

Hysteresis occurs when the ferromagnetic material is exposed to a periodic magnetization cycle. For every cycle of magnetization and demagnetization, the difference between the input and output energy is not zero. Such effect is due to the fact that the material stores energy and dissipates it as heat. The amount of this energy is proportional to the cycle area.

These losses depend on several factors such as the material, the hysteresis loop size, the peak value of the magnetic field density (B_{max}) and the frequency (f_s). Specific hysteresis losses are expressed by the *Steinmetz* formula [10] (43):

$$p_h = k_h f_s B_{max}^\zeta \quad (W/kg) \quad (43)$$

Where k_h is a material constant and ζ is the Steinmetz constant, which depends on the peak operating flux density.

Specific Eddy Current Loss

When the iron core is exposed to an alternating flux, in accordance to the *Faraday Lenz* law, emfs are induced in the conductive core material. Since the material presents a low conductivity, these voltages generate the currents in the iron, which are called *eddy* currents. In order to reduce the effect of the eddy currents, the ferromagnetic metal core is often divided in laminations. Moreover, a high resistivity compound can be used, however the overall cost increases.

The eddy current losses depend on air-gap harmonics field and they can be expressed by the following formula [10]:

$$p_{ec} = k_{ec} \sum_{n=1}^{\infty} B_{n-max}^2 (n \cdot f)^2 \quad (W/kg) \quad (44)$$

Where n is the harmonic number. k_{ec} is the loss constant that depends by the material resistivity and by the size of the current path.

In conclusion, the eddy current loss is proportional to the square of the frequency, whereas, the hysteresis loss is proportional to the frequency.

Rotor Iron Losses

In general, in the PMSM the rotor loss can be neglected, since the rotor rotates synchronously with the stator fundamental wave.

However, due to the semi-closed slots and to the non-sinusoidal phase current waveforms, harmonics frequencies are present in the airgap field. Such harmonics induce eddy currents in the rotor and even in the permanent magnet.

Therefore, the rotor losses can be calculated with Eq.(43) and Eq.(44) but changing the fundamental frequency.

Permanent magnet losses

When the permanent magnets are exposed a variable magnetic field, for the Faraday-Lenz law an emf is induced. Regarding the Figure 31, an emf is induced in each side of the magnet along its length and it is given by Eq.(45):

$$2V = \frac{d\phi}{dt} = \frac{d(BA)}{dt} \quad (45)$$

ϕ is the magnetic flux given by the product of the magnet area per the flux density.

Due to this *emfs*, an induced current flows in the magnet. This current is called eddy current and is given by (46):

$$I_{ec} = \frac{2V}{R} \quad (46)$$

Where the R is the magnet resistance, which depends on the material conductivity (σ) and the eddy current path as shows in (47):

$$R = \frac{1}{\sigma} \frac{4L}{wt} \quad (47)$$

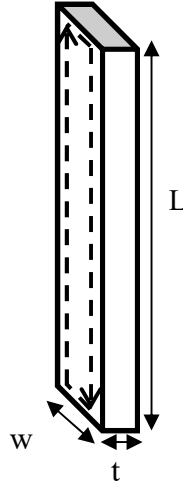


Figure 31 Eddy current path

In the end, the losses are given by (48):

$$P_{ecm} = R I_{ec}^2 \quad (48)$$

For instance, the Neodymium iron boron magnets contain high quantity of iron that implies high electric conductivity.

In order to decrease these losses, the magnets are segmented both on the axial and circumferential direction. By reducing the size of the magnet even, the losses decrease.

Mechanical Losses

Mechanical losses are composed of the two parts: bearing friction losses and windage losses.

The first contribution depends on the linear mode on the speed rotation and the load on the bearing. Usually the calculation of these losses requires an accurate analysis of the fluid mote, but in this thesis it is used an approximate formula given by [7]:

$$P_{fr} \approx \frac{1}{2} \omega \mu_b F d_b \quad (49)$$

Where ω is the mechanical angular frequency, μ_b is a coefficient due to the bearing (0.08-0.20) and d_b is the bearing inner diameter. Moreover, F is the bearing load and it is given by (50):

$$F = W_r g \quad (50)$$

Where g is the gravitational acceleration and W_r is the rotor weight.

Windage loss depends on the resistance offered by the air during the rotation. Windage losses are based on the formula given by [7]:

$$P_{wind} = C_d \pi \rho_{air} \omega_m^3 r^4 L \quad (51)$$

Where the ρ_{air} is the air density at 50°C, r_r is the rotor outer diameter, L is the active length and C_d is a coefficient that depends on the fluid speed.

This coefficient is given by Eq. (52) [11] :

$$C_d = 0.035 Re^{-0.15} \quad (52)$$

Where Re is the Reynolds Number:

$$Re = \omega r_r \rho \frac{\delta}{\nu} \quad (53)$$

δ is the air gap and ν is the cinematic viscosity of the air.

Windage losses can be significant with increasing machine speed.

3 FE Analysis

Finite Element analysis is a numerical method for computing the magnetic field distribution inside the motor. It allows a quick study of complex electromagnetic problems by solving the *Maxwell's* equations. In many cases, an analytic solution is difficult to determine, especially if the materials are non-linear.

A FE method allows the observer to determine a solution, even with non-linear materials and with time-variable fields. This method is based on the divide of the whole domain in a large number of regions with a simple geometry, namely the Finite Elements. Each element is characterized by a set of *Maxwell's* equations, relatively easy to calculate.

The combination of the system of equations allows us to achieve an approximate solution of the initial problem. The FE software discretizes the domain by using triangular elements. For an accurate analysis, a large amount of elements is needed, however it increases the computation time.

In order to decrease the computation time, the size of the elements can be different. For instance, in the electric motors, the smaller elements are near the regions where most of the energy is stored (air gap).

In the case under study, the current density J and the magnetic potential A are defined only in the axial-direction, as shown in Eq. (54):

$$\vec{J} = \begin{bmatrix} 0 \\ 0 \\ J_z \end{bmatrix}; \vec{A} = \begin{bmatrix} 0 \\ 0 \\ A_z \end{bmatrix} \quad (54)$$

In accord with the *Maxwell's* equations, the B and H fields present components only in the x - y plane [2]. For instance, B is defined as:

$$\nabla \times \vec{A} = \vec{B} = \begin{bmatrix} \frac{\partial A_z}{\partial y} \\ -\frac{\partial A_z}{\partial x} \\ 0 \end{bmatrix} \quad (55)$$

Therefore, the magnetic field is the same in each plane normal to the rotation axis. The FE analysis is computed by assuming such planar symmetry.

By neglecting the end-windings effects and using the planar symmetry of the machine, a two dimensional (2D) analysis can be studied instead of 3D. This allows to choose of a lighter processor and a shorter computation time. Some three-dimensional effects are not considered.

However, to take into account the axial segmentation of the magnets, a correction factor was introduced.

In general, the *FE* analysis is organized as follows:

- Creating a study by selecting an analysis type
- Creating geometry 2D model
- Assign materials for each part
- Assign circuit and conditions
- Study proprieties
- Generating mesh
- Post processing

The electromagnetic analysis was carried out through the *JMag software*.

3.1 2D Model

Since the current is time-variable, a magnetic transient analysis is used for the following studies. It is often combined with an *iron loss* analysis.

The motor has the parameter q not integer, therefore there is no circumferential symmetry. For this reason, a complete model must be analysed rather than a partial model.

The motor geometry was created with the *JMag Geometry Editor*.

Considering the transformation from 3D to 2D, the active length must be set in the study properties.

In the following pages the mesh detail is shown with a focus on the airgap mesh, which is the most significant part in the magnetic analysis. In fact, the smallest elements are near the air-gap, as shown in Figure 32.

The distance away from the model where the magnetic field may be considered sufficiently low is set to 1.25, it is represented in green. Such value represents a boundary condition for the problem.

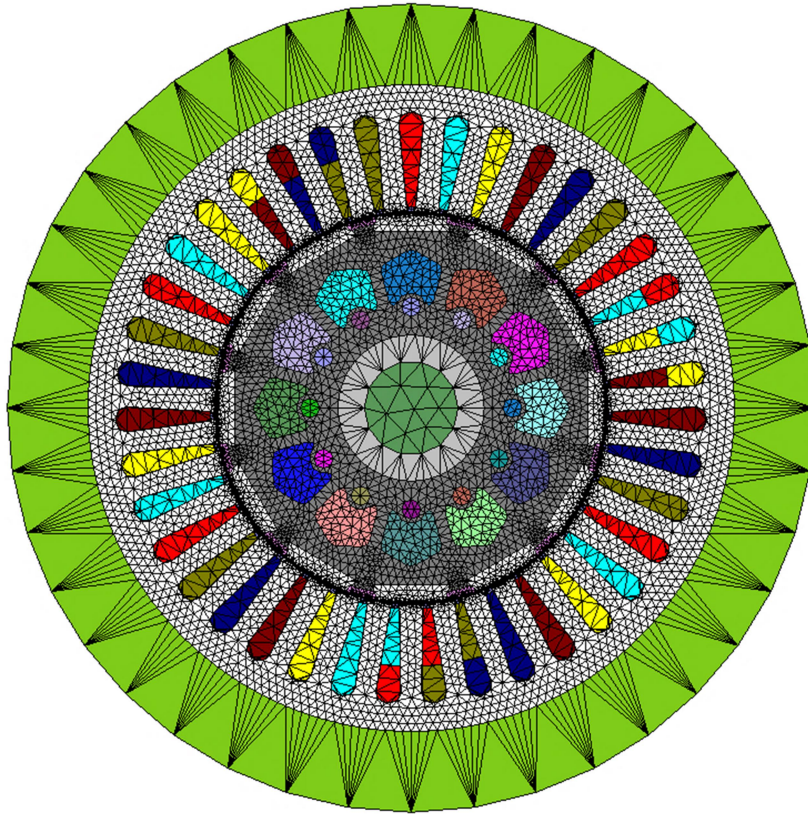


Figure 32 2D Model mesh

As is well known, the torque is expressed as a line integral of the B in the air-gap therefore, it depends on the path. In order to avoid calculation errors in the dynamic simulations, the airgap mesh must be the same during the rotor movement. This is achieved through the division of the air-gap in more radial layers.

The airgap mesh detail is exposed in Figure 33. The two white parts are the stator teeth and the magnets, the violet and the blue consist of the air region.

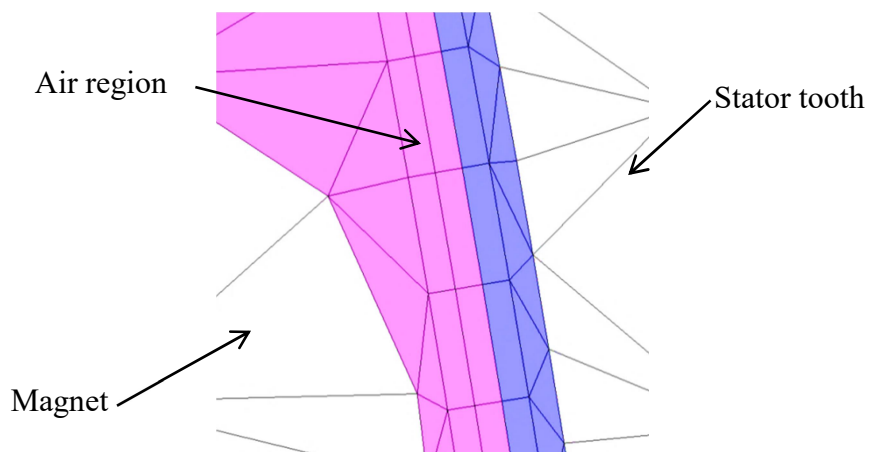


Figure 33 Radial division of the airgap mesh

3.1.1 Material

Permanent Magnets

The magnet type was calculated from the test rig results. In fact, from the expression of the magnet torque (Eq.(26)) it is possible to find the PM flux linkage:

$$\Psi_{PM} = \frac{2}{3} \frac{T}{p I_q} \quad (56)$$

The test was carried out at a mechanical speed (n) equal to 4000 rpm and the current was set only on the q -axis and equal to 360 A.

The average torque achieved is equal to $T=43$ Nm. Therefore, the peak value of the flux linkage is:

$$\Psi_{PM} \approx 0.0133 \text{ Wb} \quad (57)$$

In order to find the magnet type several simulations FEM were evaluated. The result is the *NEOMAX-37SH* from *Hitachi Metals*. Such a component allows us to achieve the same mechanical performance, as illustrated in the next subsection.

Figure 34 shows the magnet performance depending on operating temperature.

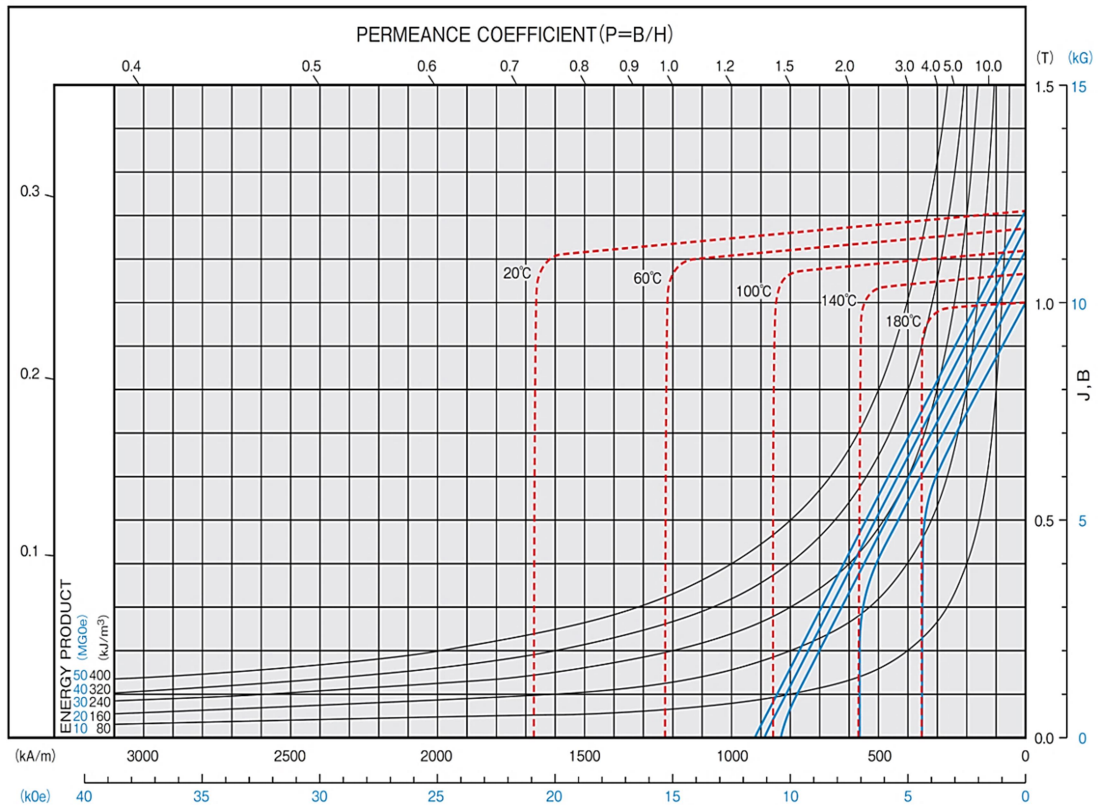


Figure 34 Normal Curve of Neomax 37SH (Source: Hitachi Metals)

The magnetization pattern is set according to Figure 21.

Stator and Rotor Core

In the FEM model, NO20 lamination steel is employed for the following elements: rotor core, stator teeth and stator yoke.

Table 12 shows the mechanical and physical proprieties of NO20.

Parameter	Value
Nominal Thickness	0.20 mm
Resistivity	52 $\mu\Omega\text{cm}$
Thermal Conductivity	28 W/m K
Specific Heat	1900 J/kg K
Density	7650 kg/m ³

Table 12 NO20 Physical Proprieties

Table 13 and Figure 35 show the first magnetization curve.

B (T)	H (A/m)	B (T)	H (A/m)
0	0	1	91
0.1	29	1.1	111
0.2	36	1.2	145
0.3	42	1.3	214
0.4	46	1.4	411
0.5	51	1.5	1280
0.6	55	1.6	2970
0.7	61	1.7	5380
0.8	68	1.8	9390
0.9	78		

Table 13 Magnetization curve of NO20 at 50Hz

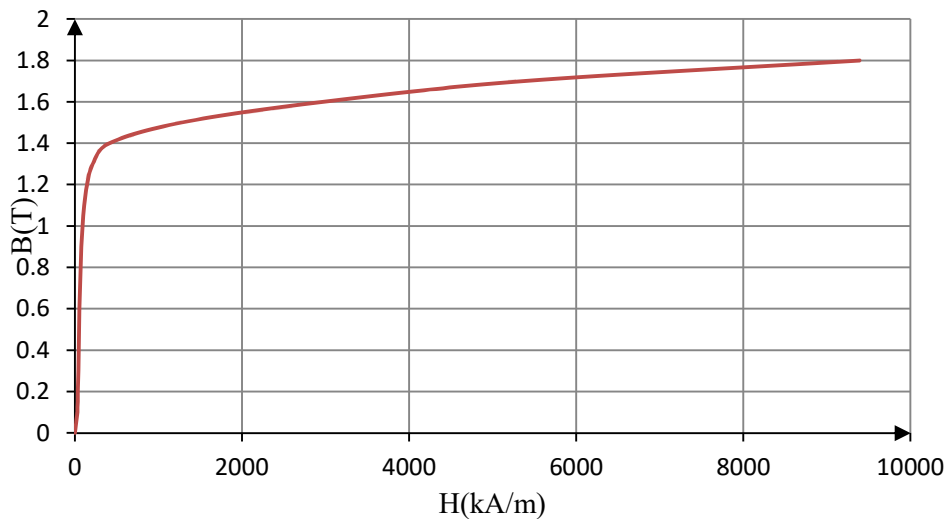


Figure 35 Magnetization curve of NO20 at 50Hz

Table 14 and Figure 36 show the specific total loss for hysteresis depending on B and on the frequency.

Polarization B(T)	Specific Total Loss (W/kg)				
	at 50 Hz	at 400Hz	at 2500 Hz	at 5000 Hz	at 10000 Hz
0.1	0.02	0.17	2.79	9.01	27.0
0.2	0.07	0.72	10.6	31.8	95.6
0.3	0.14	1.49	24.4	65.6	191
0.4	0.23	2.50	40.4	108	315
0.5	0.32	3.80	58.4	159	
0.6	0.42	5.17	78.4	219	
0.7	0.54	6.70	103	290	
0.8	0.66	8.36	133	375	
0.9	0.8	10.3	166	477	
1.0	0.95	12.3	200		
1.1	1.14	14.8	248		
1.2	1.36	17.9			
1.3	1.65	21.4			
1.4	2.00	25.3			
1.5	2.40	29.7			
1.6	2.75				
1.7	3.06				
1.8	3.32				

Table 14 Specific total loss for hysteresis depending on B and frequency

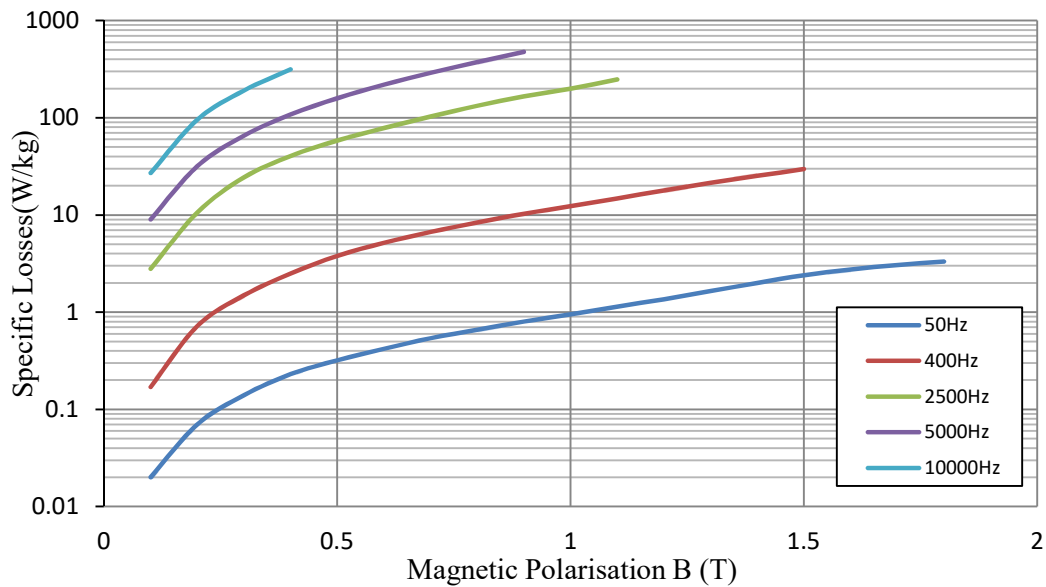


Figure 36 Specific loss B (f)

The NO20 material was created since it was not registered within JMag library.

In addition, the winding are made of copper.

3.2 Circuit

The entire electric circuit is composed of the three phase current source, the star connection and the magnet FEM conductors, as shown in Figure 37a.

The parameters of the current (amplitude, phase angle, frequency) can be set up by means of the three phase current source.

Figure 37b shows the sub-circuit within the star connection block. For each FEM-coil was inserted the resistance value and the number of turns.

In addition, a FEM conductor was set up for each magnet, to take into account the eddy current for a 2D model. As for the settings of the circuit, the left terminal of each *fem* is in open-circuit whereas the right terminal is connected to the ground circuit.

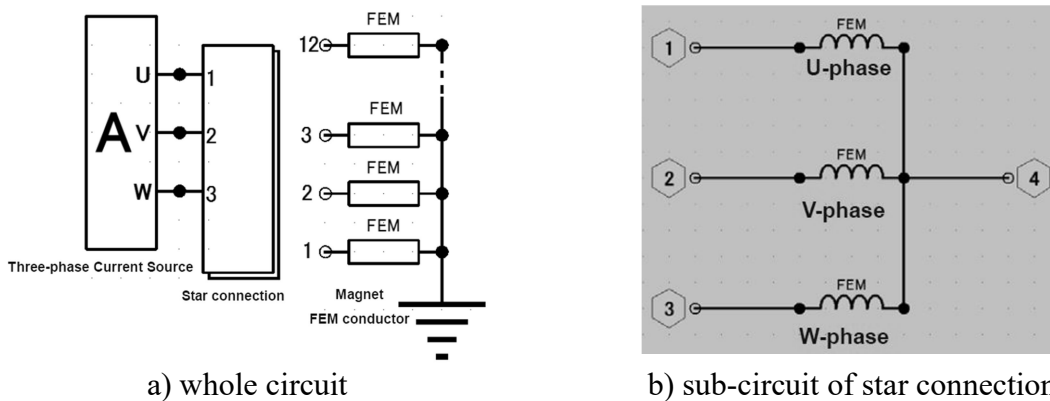


Figure 37 Electric circuit

3.2.1 Alignment of the Rotor with the Stator

The electric circuit illustrated above, works on a three-phase reference system ($u-v-w$). Before starting the analysis, it is mandatory to set the alignment between the d-axis (rotor reference axis) and the magnetic axis of the u-phase (stator reference system).

A possible approach is based on the *No-load* simulation, where the phasor of the stator voltage must be on the q-axis, as results from Eq.(58) :

$$U_{s0} = \sqrt{U_{d0}^2 + U_{q0}^2} = U_{d0} = \omega \Psi_{pm} \quad (58)$$

Simulation is performed at:

- $n=4500$ rpm
- Initial angle of the rotor = 0°
- Current amplitude = $0A$; Current phase angle = 0° .

By analysing the *u-phase* voltage, if the relative phase-angle is zero the stator reference system is coincident with the rotor reference system. Otherwise, the stator reference system has to be rotated by an electric angle.

That angle corresponds to the offset of the fundamental harmonic of the *u-phase* voltage, which is derived through the *FFT* (Fourier Fast Transform). Since the FFT is expressed as a sum of cosines whereas the reference system as a function of the sine, at the angle is added 90°.

Figure 38a shows the reference systems where the *d-axis* and *u-phase* axis are unaligned while in Figure 38b the *d-axis* is coincident with the *u-phase* axis.

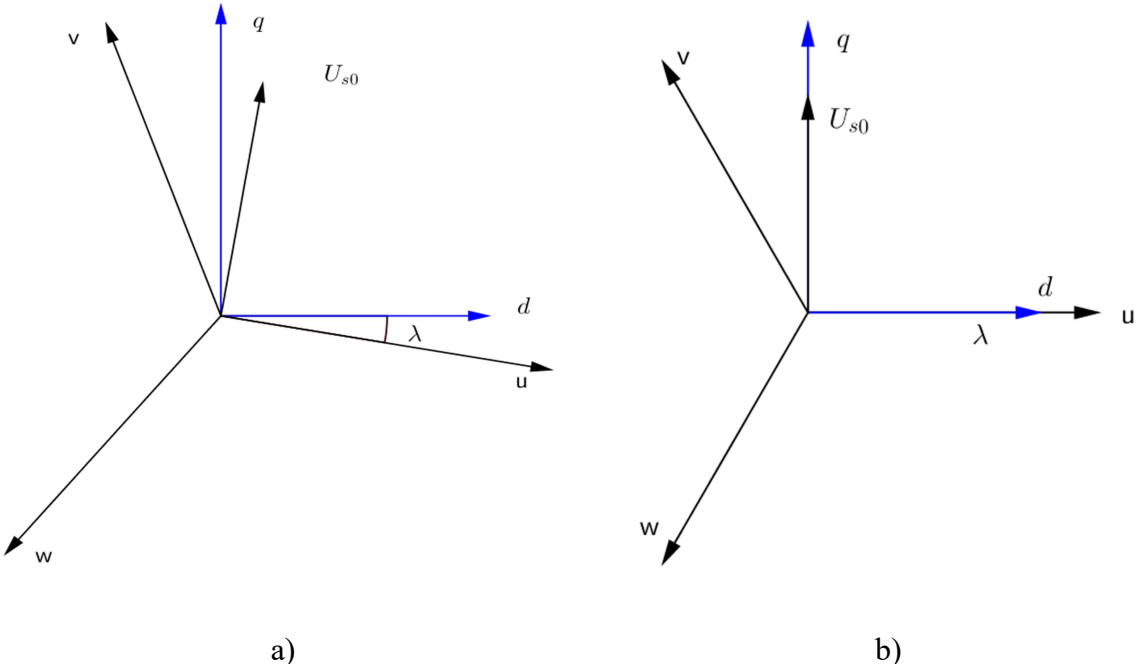


Figure 38 Rotor position respect stator reference uvw

Table 15 shows the amplitude and the phase of the fundamental harmonic of the no-load voltage.

	Frequency (Hz)	Amplitude (V)	Phase (°)
U_{u1}	450	38.49	-8.169

Table 15 FFT No-Load voltage

In addition, from the no load simulation, the maximum PM flux linkage was calculated.

$$\psi_{PM} = 0.0135 \text{ Wb}$$

This is approximately the value carried out from the test (see Eq.(57))

Figure 39 shows the no-load voltage.

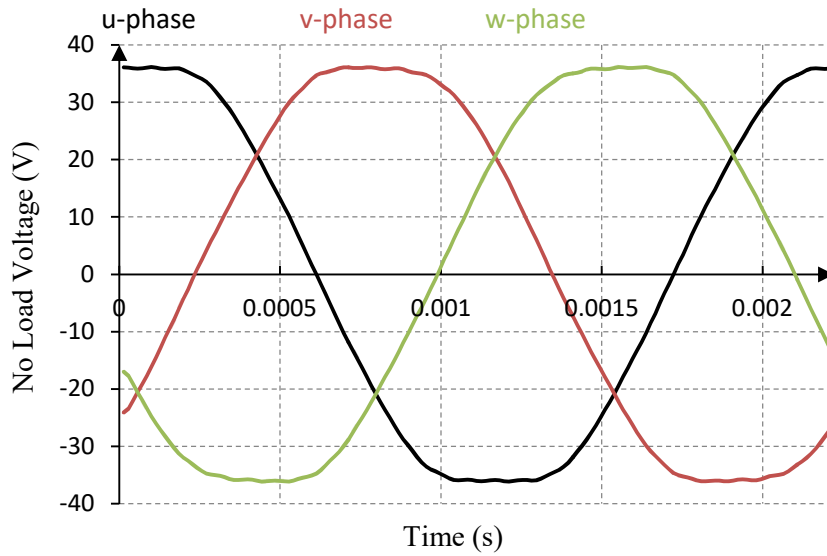


Figure 39 No-load voltage

3.3 Nominal Point

In order to determinate the direct and quadrature axis inductances, a simulation with nominal value was carried out.

The simulation is performed with the following parameters:

- $I_n=207.1 A_{rms}$
- $n_n=8900 rpm$

From the analysis, the average torque results equal to 35.18 Nm. The error between the FEM model and the datasheet value is:

$$e_{\%} = \frac{T_n - T_{nFEM}}{T_n} \cdot 100 = \frac{35.82 - 35.18}{35.82} \cdot 100 = 1.78\%$$

Figure 40 shows the torque curve at nominal point.

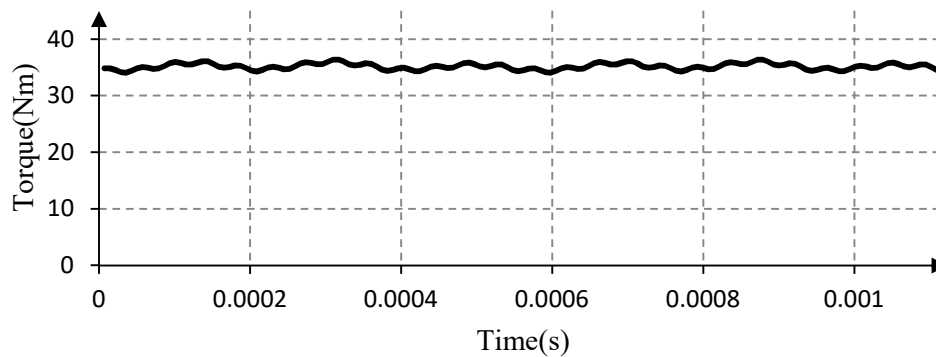


Figure 40 Nominal torque

3.3.1 Inductances of Direct and Quadrature axis

The value of the inductances can be calculated from the flux equation:

$$\begin{cases} \psi_{sd} = L_d I_d + \psi_{PM} \\ \psi_{sq} = L_q I_q \end{cases} \quad (59)$$

PM flux linkage is obtained from the *No Load voltage* simulation ($I_d = 0$; $I_q = 0$).

Afterwards the value of L_d is computed when the $\psi_{sq} = 0$, namely when $I_q = 0$.

$$L_d = \frac{\psi_{sd} - \psi_{PM}}{I_d} \quad (60)$$

In addition, the L_q is calculated by setting the $I_d = 0$.

$$L_q = \frac{\psi_{sq}}{I_q} \quad (61)$$

JMag Inductance tool was used to carry out a multi-case transient magnetic field analysis depending on the current amplitude. The tool is based on the theory mentioned above. The magnetic fluxes on both axes are calculated. The range of current amplitude is set up from 0.1 I_n to I_n at the rated speed (8900 rpm).

Table 16 and Figure 41 show the results.

Amplitude (A)	Ld (μ H)	Lq (μ H)	Lq/ Ld
29.2	22.07	27.66	1.25
58.4	23.04	27.81	1.21
87.6	23.65	27.91	1.18
116.8	24.01	27.95	1.16
146	24.20	27.98	1.16
175.2	24.25	27.98	1.15
204.4	24.30	27.95	1.15
233.6	24.32	27.89	1.15
262.8	24.33	27.83	1.14
292	24.34	27.77	1.14

Table 16 Inductance table

The inductances of the q -axis and d -axis are slightly different since the magnets are not completely surface mounted, as shown in Figure 42 . The reason is that the magnetic flux on d -axis passes through the magnet with low permeability. While the magnetic flux on q -axis passes through a path with more iron and then less reluctance.

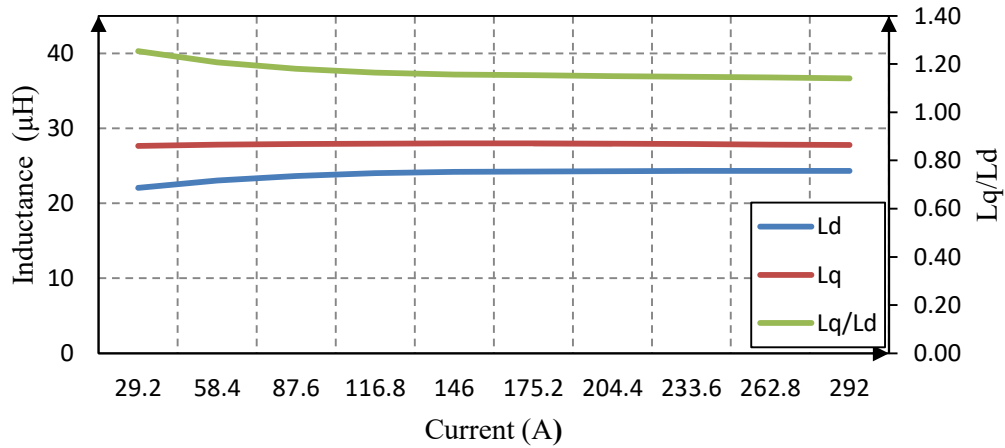


Figure 41 Inductance depending on electrical angle

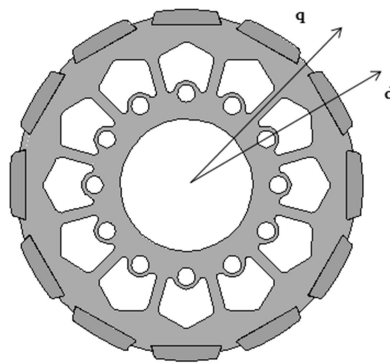


Figure 42 Rotor

3.4 Maximum Torque

The aim of the simulation is to check if with the materials employed in the simulation, the machine achieves the maximum value of the torque. The simulation is performed at:

- maximum current $I_{MAX}=500A_{rms}$
- base speed $n=4500$ rpm

The result is shown in Figure 43.

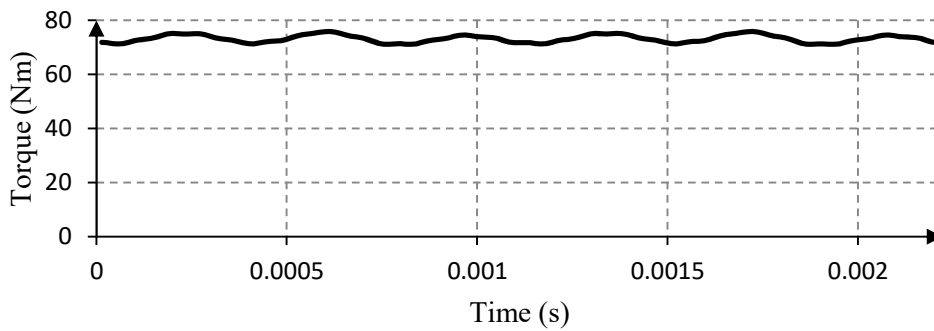


Figure 43 Maximum torque

The average value is $T_{MAX}=73.14$ Nm.

The error between the FEM model and the datasheet value is:

$$e_{\%} = \frac{T_{MAX} - T_{MAX_{FEM}}}{T_{MAX}} 100 = \frac{74.6 - 73.14}{74.6} 100 = 1.95\%$$

3.5 Post Process-Iron Loss study

As already written, the iron losses depend on the peak value of the magnetic flux density B and they increase when the frequency rises.

In order to evaluate the iron losses results, a transient magnetic field analysis model was carried out. From the result, it was obtained a time history of the magnetic flux density distribution. Therefore, the electromagnetic transient analysis is linked with an iron-loss analysis.

Since the rotor losses are not induced by the stator fundamental wave, but from higher space harmonics, two different iron loss studies were created.

The fundamental frequency for evaluating the stator iron losses is given by Eq.(62):

$$f_s = \frac{n}{60} p \text{ (Hz)} \quad (62)$$

Regarding the rotor loss, the frequency is a function of the slots number:

$$f_r = \frac{n}{60} Q \text{ (Hz)} \quad (63)$$

In addition, a correction factor is introduced in the iron losses, to take into account the punching process during the manufacturing of the laminated steel [12].

For this reason, the FEM results of the iron losses are multiplied for the punching factor.

Part	Punching factor
Stator yoke	1.6
Stator teeth	1.8
Rotor	1.6

Table 17 Punching factor

Eddy Current Loss in Permanent Magnet

Since the model was analysed in 2D, a correction factor is introduced in the material conductivity to take into account the magnet segmentation in the axial direction.

$$\sigma' = F \sigma \quad (64)$$

The correction factor (F) was developed by [13] and it is based on the ratio between the power losses in the 3D model and in the 2D model:

$$F = \frac{P_{3D}}{P_{2D}} = \frac{3}{4} \frac{a^2}{w^2 + a^2} \quad (65)$$

Where a and w are the length and the medium width of the magnet respectively.

Parameter	Value	Unit
a	16.5	mm
w	17	mm
F	0.458	
σ	$0.667 \cdot 10^6$	S/m
σ'	$0.323 \cdot 10^6$	S/m

Table 18 Magnet correction factor

3.6 Efficiency Map

The efficiency describes how an electric motor transforms the electric power into mechanical power. In Europe it was developed a new efficiency energy standard, by the *International Electrotechnical Commission* (IEC), in order to have a universal definition of efficiency. The procedure name is IEC 60034-30-2. It concerns all motor technologies, power ranges from 0.12 kW to 1000 kW. The main disadvantage is that with this procedure can be estimate the energy efficiency only in the constant torque operation ($n < 4500 \text{ rpm}$) [14]. To create the efficiency map from the measurements it is necessary from 100 to 1000 operating- points.

The interpolation formula of Prof. *Doppelbauer* allows us to determinate the efficiency map from the power analysis of only seven points. As already shown, the losses depend on the frequency and on the torque (it is a function of the current).

In general, they can be expressed as [8]:

- Stator Winding : $P_{sw}(f, T) = P_{sw}(f_n, T_n) \frac{l_0}{l_n} + P_{sw}(f_n, T_n) \left(1 - \frac{l_0}{l_n}\right) T^2$
- Iron Losses: $P_{fe}(f, T) = \frac{1}{2} P_{fe}(f_n, T_n) f + \frac{1}{2} P_{fe}(f_n, T_n) f^2$
- Additional Losses: $P_{LL}(f, T) = \frac{1}{2} P_{LL}(f_n, T_n) T^2 + \frac{1}{2} P_{LL}(f_n, T_n) T^2 f^2$
- Friction and Windage losses : $P_{fw}(f, T) = \frac{1}{2} P_{fw}(f_n, T_n) f + \frac{1}{2} P_{fw}(f_n, T_n) f^3$
- Additional harmonic losses: $P_{HL}(f, T) = P_{HL}(f_n, T_n)$

In conclusion, the total losses are given by:

$$P_L(f, T) = P_{sw}(f, T) + P_{fe}(f, T) + P_{LL}(f, T) + P_{fw}(f, T) + P_{HL}(f, T)$$

The efficiency can be calculated from:

$$\eta(f, T) = \frac{P_m}{P_m + P_L} = \frac{f T}{f T + P_L(f, T)}$$

Where P_m is the mechanical power.

In addition, the power losses can be written as a function of seven coefficients:

$$P_L(f, T) = A + B f + C f^2 + D f T^2 + E f^2 T^2 + F T + G T^2$$

The relations proposed above are valid only in linear zone. Therefore, the flux-weakening region cannot be evaluated since the motor could work in saturation.

Regarding the constant torque region, all quantities are related to the following values:

- $T=1$ rated torque (35.82 Nm)
- $n=1$ base speed (4500 rpm)

The seven points necessary for the interpolation are shown in Table 19

	f (Hz/450)	T (Nm/35.82)
P ₁	0.9	1
P ₂	0.5	1
P ₃	0.9	0.5
P ₄	0.5	0.5
P ₅	0.25	1
P ₆	0.5	0.25
P ₇	0.25	0.25

Table 19 7 Operating points for efficiency map

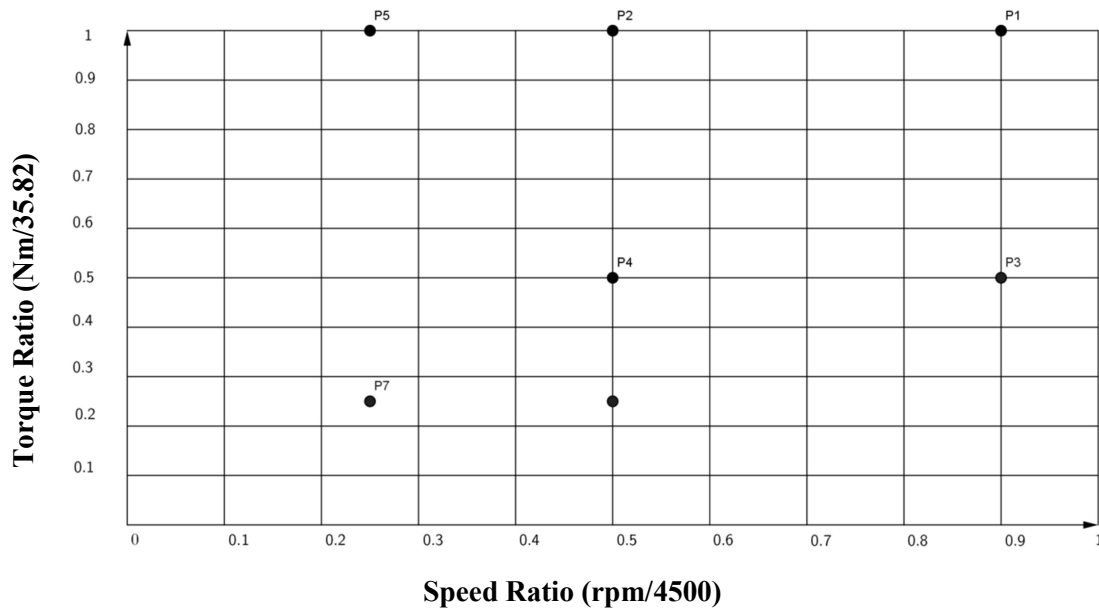


Figure 44 7 Points efficiency map

The maximum frequency is set to 0.9 to avoid the voltage drop at the frequency converters. [14] . From the losses of these 7 points, it is possible to find the coefficients of the interpolation.

$$\begin{pmatrix} P_{L1} \\ P_{L2} \\ P_{L3} \\ P_{L4} \\ P_{L5} \\ P_{L6} \\ P_{L7} \end{pmatrix} = M \begin{pmatrix} A \\ B \\ C \\ D \\ E \\ F \\ G \end{pmatrix}$$

$$\begin{pmatrix} A \\ B \\ C \\ D \\ E \\ F \\ G \end{pmatrix} = M^{-1} \begin{pmatrix} P_{L1} \\ P_{L2} \\ P_{L3} \\ P_{L4} \\ P_{L5} \\ P_{L6} \\ P_{L7} \end{pmatrix}$$

Where M is:

$$M = \begin{bmatrix} 1 & 0.9 & 0.81 & 0.9 & 0.81 & 1 & 1 \\ 1 & 0.5 & 0.25 & 0.5 & 0.25 & 1 & 1 \\ 1 & 0.9 & 0.81 & 0.225 & 0.2025 & 0.5 & 0.25 \\ 1 & 0.5 & 0.25 & 0.125 & 0.0625 & 0.5 & 0.25 \\ 1 & 0.25 & 0.0625 & 0.25 & 0.0625 & 1 & 1 \\ 1 & 0.5 & 0.25 & 0.03125 & 0.015625 & 0.25 & 0.0625 \\ 1 & 0.25 & 0.0625 & 0.015625 & 0.00390625 & 0.25 & 0.0625 \end{bmatrix}$$

In this work, the *additional* losses and *harmonic* losses are neglected and the overall results are listed in Table 20.

	$P_{sw}(W)$	$P_{fe}(W)$	$P_{fw}(W)$	$P_L(W)$
P _{L1}	598.22	196.42	39.02	825.97
P _{L2}	598.22	86.06	14.86	694.30
P _{L3}	149.56	180.25	39.02	355.30
P _{L4}	149.56	79.04	14.86	237.15
P _{L5}	598.22	35.75	6.29	637.66
P _{L6}	37.39	78.31	14.86	123.61
P _{L7}	37.39	32.35	6.29	73.02

Table 20 7 Operating points: power losses

The coefficients are:

A	2.3953
B	115.5623
C	137.9624
D	3.9287
E	31.9324
F	-6.5599
G	604.3218

Table 21 Interpolation coefficients

In the Appendix A the Matlab code implemented for the efficiency map is shown.

Figure 45 shows the efficiency map calculated with the 7 points procedure.

It can be observed from the Figure 45 that, the motor exhibits efficiency greater to 89% in the range of torque over 5 Nm and speed over 500 rpm. At low speed and high torque, the efficiency is low, since to achieve such torque, a high current is needed. Therefore, high copper losses.

In addition, at low torque and high speed, the mechanical and the iron losses are high. As well known, these components depend on the mechanical speed, namely on the input frequency.

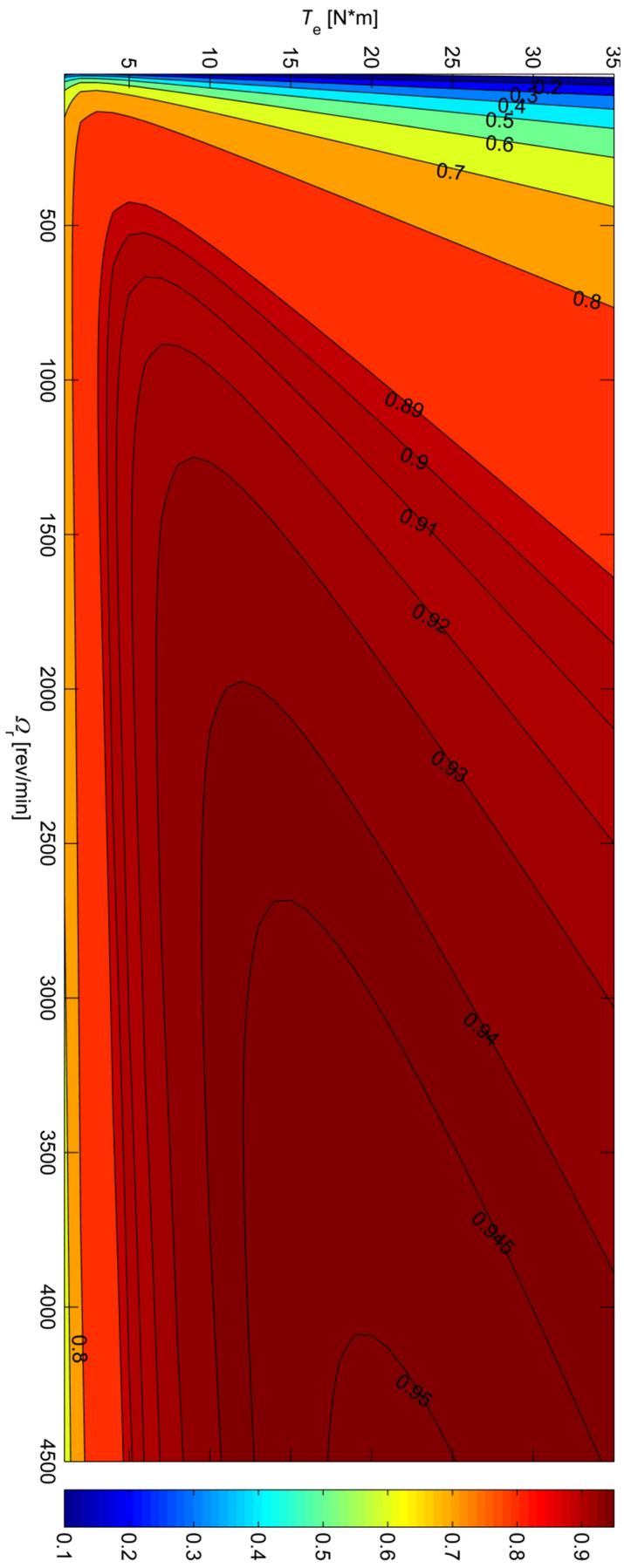


Figure 45 Efficiency map

3.7 FE Analysis of Losses as a Function of Current Phase Angle

In the constant torque region, the motor is often controlled to maximize the torque for the given current, known as MTPA (maximum torque per Ampere). The torque expression was obtained in the Subchapter 1.3

$$T_e = \frac{3}{2}p\psi_{PM}I_q + \frac{3}{2}p(L_d - L_q)I_dI_q \quad (66)$$

In this case, the torque is mainly due to the permanent magnet, given that the term $L_d - L_q \cong 0$. Therefore, the influence of the d-current on the torque production is low. In order to minimize the copper losses in the MTPA, that current is set to zero ($I_d = 0$).

However, the iron losses can be changed by the current on the d-axis.

The aim of this subchapter is to evaluate the iron losses as a function of the current phase angle.

Starting from the flux equation in the d-q reference system:

$$\psi_s = \sqrt{\psi_{sd}^2 + \psi_{sq}^2} = \sqrt{(\psi_{PM} + L_d I_d)^2 + (L_q I_q)^2}$$

Where, as well known:

$$\begin{cases} I_d = I_s \cos(\beta) \\ I_q = I_s \sin(\beta) \end{cases}$$

Figure 46 shows the phasor diagram when the machine works with $I_d = 0$. In this case, the stator flux linkage is due to the term of the permanent magnet and to the flux on the quadrature axis.

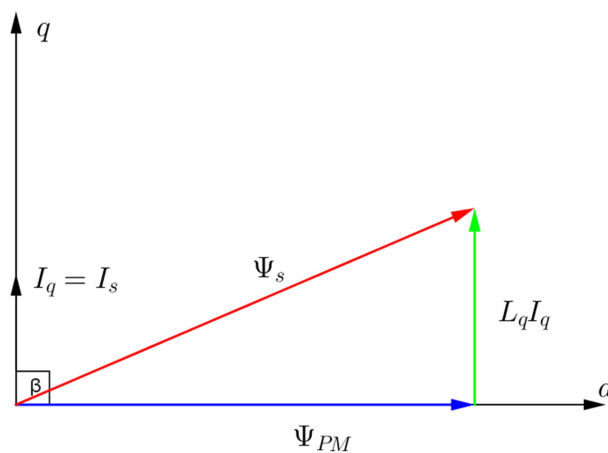


Figure 46 Phasor diagram with $I_d=0$

Keeping constant the magnitude of the stator current and by increasing β , the stator flux decreases. This is due to the demagnetization effect of the d-current (violet line in Figure 47). Therefore, even the magnetic flux density in the air-gap decreases.

A new operating point is represented with the superscripts.

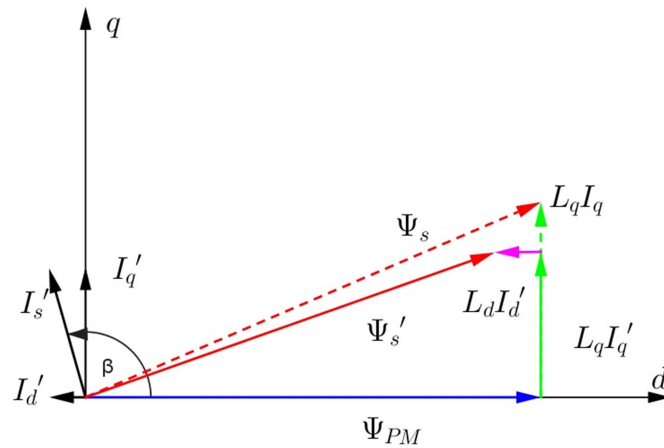


Figure 47 Phasor diagram with $I_d \neq 0$

3.7.1 Simulation Results

The simulation is performed at:

- $n=4000$ rpm
- $I_{rms} = 255 A_{rms}$
- Current phase angle $\beta=[90 \div 150]$

The torque and losses are evaluated as a function of current phase angle.

As shown in Table 22, by increasing the angle β , initially the torque shows a slight increment due to the reluctance torque. Over 120° , the torque value rapidly declines.

Angle β ($^\circ$)	Torque(Nm)	P_{mecc} (kW)
90	41.66	17.451
100	42.62	17.851
110	42.11	17.637
120	40.03	16.766
130	36.37	15.236
140	31.25	13.089
150	24.86	10.413

Table 22 Torque as a function of current phase angle ($n=4000$ rpm; $I=255A_{rms}$)

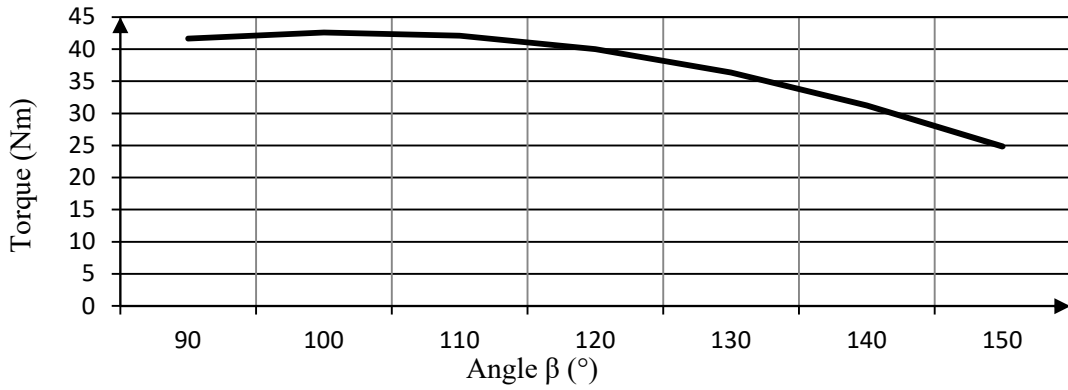


Figure 48 Torque depend on current β ($n=4000$ rpm; $I=255A_{rms}$)

Table 23 shows the iron losses in the rotor, the stator and the permanent magnet

Angle β (°)	Hysteresis Losses			Eddy Current Losses			
	Rotor (W)	Teeth (W)	Yoke (W)	Rotor (W)	Teeth (W)	Yoke (W)	PM (W)
90	4.022	108.48	38.443	0.398	94.860	44.728	8.172
100	5.703	95.033	34.394	0.431	89.900	40.254	7.918
110	6.709	81.370	29.648	0.401	82.827	34.773	7.599
120	7.053	68.579	24.579	0.334	73.736	28.843	7.237
130	7.453	57.457	19.520	0.193	63.302	22.785	6.818
140	8.034	47.888	14.867	0.197	52.734	17.159	6.341
150	8.086	39.986	10.844	0.233	42.321	11.416	5.833

Table 23 Iron Losses depend on β ($n=4000$ rpm; $I=255A_{rms}$)

Since the simulations are performed at constant mechanical speed and at constant current amplitude, the mechanical and Joule losses do not change.

Next, the graphs of losses are shown.

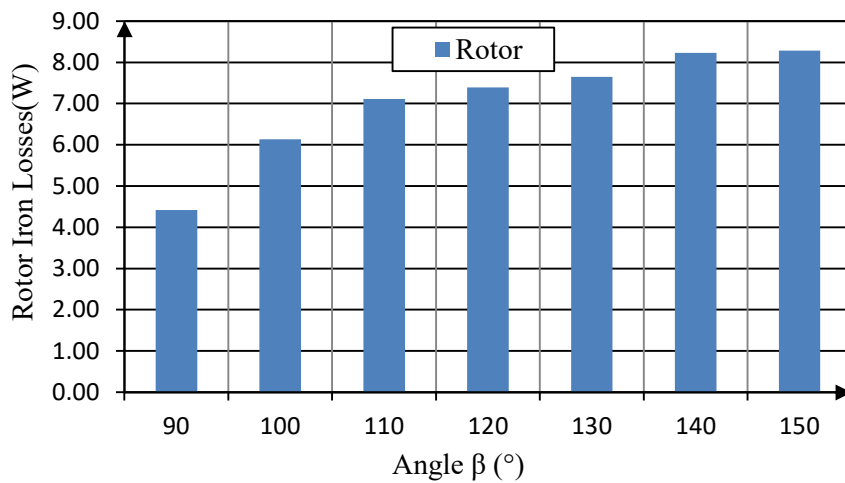


Figure 49 Rotor Iron Losses depend on β

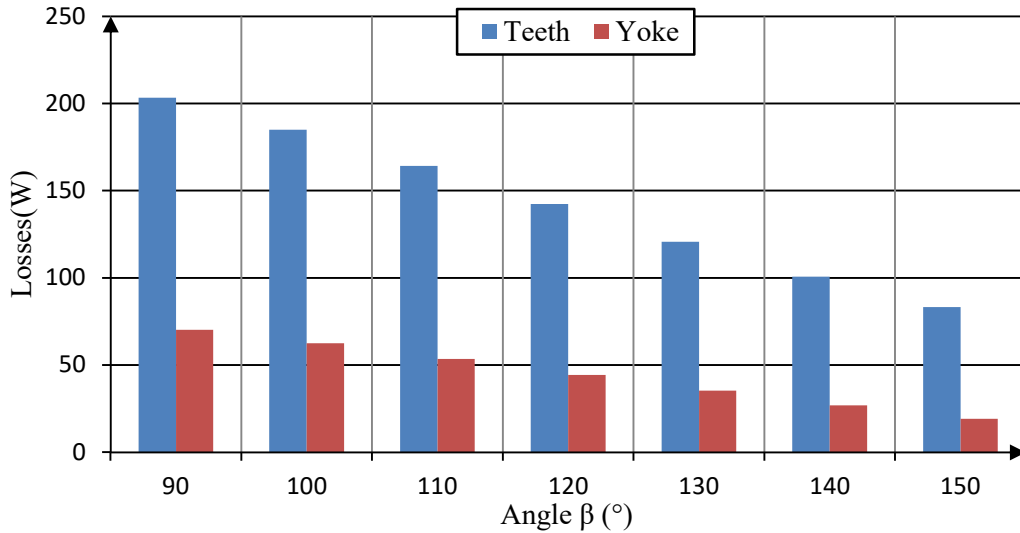


Figure 50 Stator Iron Losses depend on β

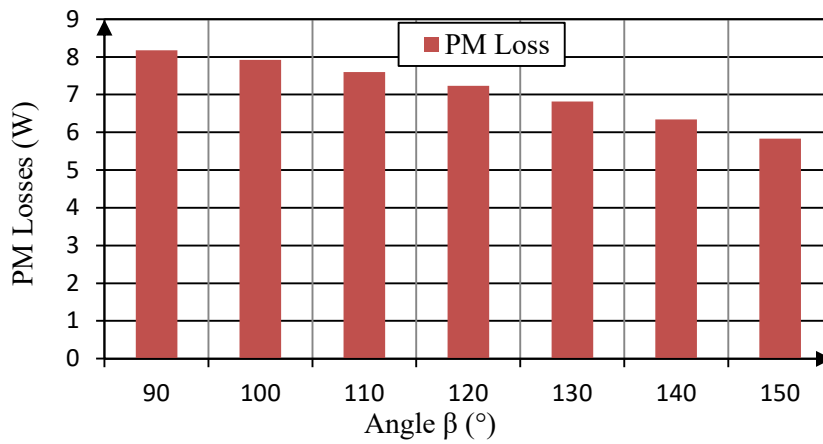


Figure 51 PM Losses depend on β

Figure 50 shows the diminution of the stator iron losses regarding on the current angle. The losses decrease of 67.36 W from $\beta = 90^{\circ}$ to $\beta=110^{\circ}$. However, the rotor iron losses slightly increase as shown in Figure 49. This is probably due to the fact that the flux is moved from the stator to the air-gap by means of the negative current I_d . Therefore the B in the rotor rises. The overall results exhibit that is possible to lower the stator losses, but raise the rotor losses, by increasing β , namely the negative d-current. However, the rise of the losses in the rotor and in the PM can be neglected.

Next, the table and figure of the overall results are shown.

Angle (β)	Copper (W)	Windage (W)	Friction (W)	Stator (W)		PM (W)	Rotor (W)
				Teeth	Yoke		
90	806.760	0.900	0.753	203.344	70.233	8.172	4.420
100	806.760	0.900	0.753	184.933	62.437	7.918	6.134
110	806.760	0.900	0.753	164.197	53.499	7.599	7.109
120	806.760	0.900	0.753	142.315	44.387	7.237	7.387
130	806.760	0.900	0.753	120.759	35.304	6.818	7.646
140	806.760	0.900	0.753	100.622	26.912	6.341	8.231
150	806.760	0.900	0.753	83.263	19.236	5.833	8.281

Table 24 Losses depend on current phase angle (n=4000 rpm; I=255A_{rms})

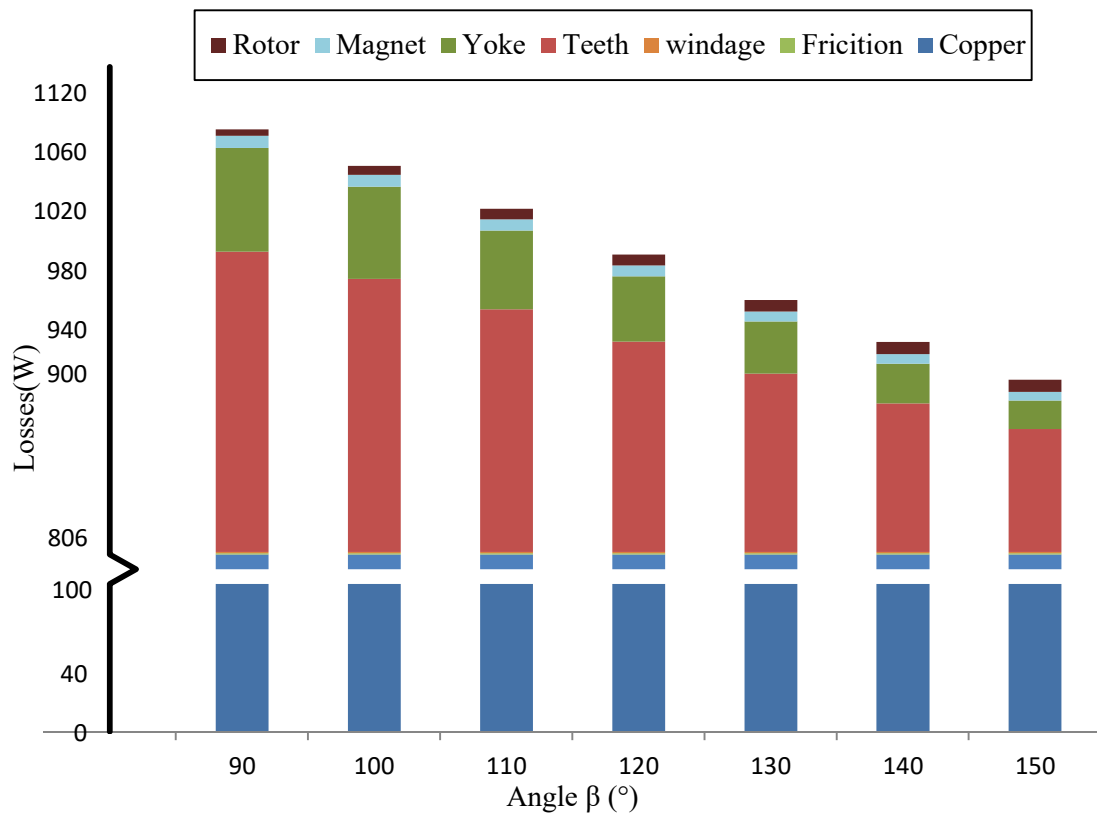


Figure 52 Overall losses regarding on the β angle

Figure 53 shows the comparison between the torque trend and the losses, when the current phase angle increases.

It can be observed from Figure 53 that, for current phase angle between 100° and 110° , the torque increases slightly while the overall losses decrease.

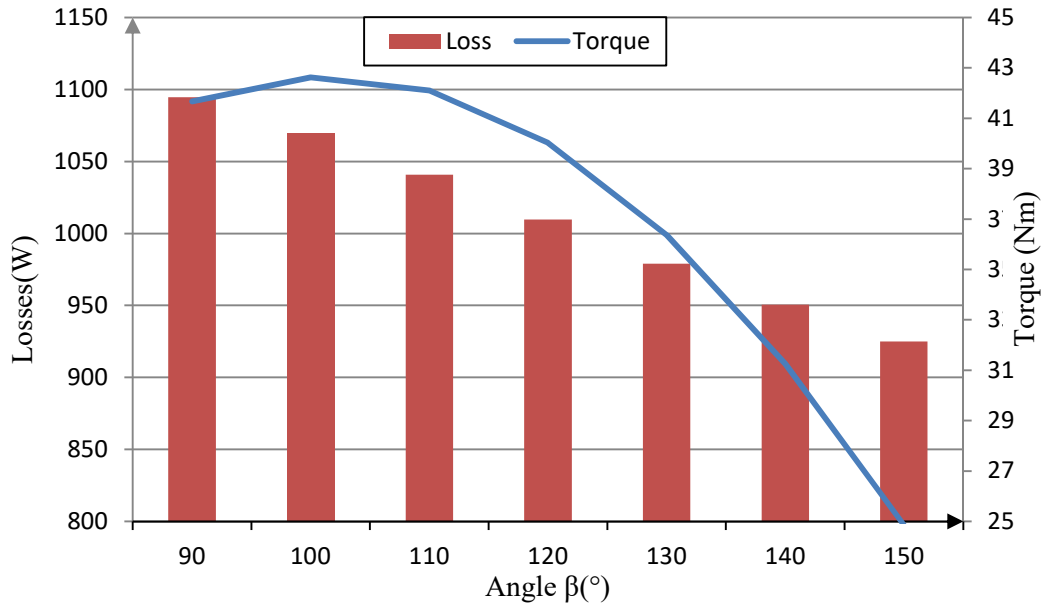


Figure 53 Overall losses vs Torque regarding on the β

The torque rise and power diminution are calculated with respect to the standard operating point $\beta=90^\circ$.

$$\Delta T = \frac{T_x - T_{90}}{T_x}$$

$$\Delta P_l = \frac{P_{l_x} - P_{90}}{P_{l_x}}$$

Table 25 shows as an increasing of the angle with respect to the strategy of MTPA, an increment of the torque with less losses is achieved.

In particular, as shown in Figure 53, using an angle beta of 110° the best compromise between torque generated and losses is obtained.

Angle β (°)	Torque (Nm)	Power Loss (W)	ΔT (Nm)	ΔP_l (W)	ΔT %	ΔP %
90	41.66	1094.58	-	-	-	-
100	42.62	1069.83	0.96	-24.75	+2.25	-2.31
110	42.11	1040.82	0.45	-53.76	+1.07	-5.17

Table 25 Comparison of results

4 Thermal Analysis

Different approaches are used to determinate the temperature behaviour in the electric motors. The Lumped Parameters Thermal Network (*LPTN*) is one of the most used methods. It allows the prediction of the temperature rising in particular points. This method is based on the analogy between the thermal and electrical networks as shown in the following equation:

$$I = \frac{V}{R} + C \frac{dV}{dt} \Rightarrow P = \frac{\theta}{R_{th}} + C_{th} \frac{d\theta}{dt} \quad (67)$$

In Table 26 the main analogies are listed.

Electric	Symbol	Unit	Thermal	Symbol	Unit
Current	I	A	Heat Flow	P	W
Voltage	V	V	Temperature	θ	K
Electric Resistance	R	Ω	Thermal Resistance	R_{th}	K/W
Capacitance	C	F	Heat Capacity	C_{th}	J/K
Current density	J	A/m ²	Heat flux density	q	W/m ²

Table 26 Analogy between thermal and electric circuit

In general, the thermal network required for such analysis is complicated. By means the geometrical symmetries in the machine, the complexity of the network is reduced.

In the cylindrical electric motor the radial, the axial and the circumferential temperature behaviours can be analysed. Since the aim of the thesis is the analysis of PM's temperature, the only radial vector is considered. Such consideration is obtained with the assumption that the three behaviours are independent from each other. The electrical machine is divided geometrically into 8 parts or nodes. Each node is connected to a heat capacity, heat source and thermal resistances for the interconnection to other nodes.

The elaboration of the thermal network can be divided into four parts:

- selection of the nodes;
- calculation thermal parameters;
- introduction of the losses as input;
- simulation of temperature behaviour.

The nodes are listed in Table 27:

1	Frame
2	Stator Yoke
3	Stator Teeth
4	Stator Winding
5	Airgap
6	Permanent Magnet
7	Rotor
8	Shaft

Table 27 Thermal nodes

In order to calculate the different resistances, the kind of heat transfer between conduction and convection has to be analysed. In this study, the radiation is neglected.

4.1 Mechanisms of Heat Transfer- Conduction

Conduction is the heat transfer through solid parts and follows the Fourier's law:

$$\vec{q} = -\lambda \nabla \vec{\theta} \left[\frac{W}{m^2} \right] \quad (68)$$

Where q is the vector of heat flux density and λ is the *thermal conductivity* that is a material characteristic. The material is called a conductor if the thermal conductivity is high otherwise it is called an insulator. The sign of the equation is in accord with the second law of thermodynamic. In the studied case, the only radial direction is defined as:

$$q_r = -\lambda \frac{d\theta}{dr} \left[\frac{W}{m^2} \right] \quad (69)$$

With the electrical analogy, the equation is converted in electrical parameters:

$$\theta_1 - \theta_2 = \Delta\theta = R_{th} P \quad (70)$$

Where R_{th} is connected to the geometry. For a mono-directional heat transfer in a cylindrical wall it is equal to:

$$R_{th} = \frac{r_1 - r_2}{\lambda S} \quad (71)$$

4.1.1 Convection

Convection is the heat transfer between a solid surface and a fluid. Convection can be classified as:

- Natural convection: when the fluid motion is due only by the temperature gradient;
- Forced convection: when the relative motion between fluid and surface is induced by an external source.

The convection is expressed by an empirical formula:

$$q = \alpha(\theta_s - \theta_r) \quad (72)$$

Where θ_s is the surface temperature and θ_r is the temperature of the undisturbed fluid. α is the coefficient and it depends on the fluid speed close to the surface, physical proprieties (viscosity, specific heat and density) of the fluid and the geometry of the system. For the convection, the thermal resistance is expressed as:

$$R_{th} = \frac{1}{\alpha S} \quad (73)$$

Between the cooling jacket and the frame and across the air-gap are the two convections in the electrical machine.

4.1.2 Heat Storage

The capacity of an object to store heat is described by its thermal capacitance. The thermal capacitance (C) of a solid part is a function of the specific heat (c) of the material and of the mass (m). The general formula is given by:

$$C = m c \quad (74)$$

4.2 General Cylindrical Component

This thermal analysis is based on the following assumptions [9]:

- the circumferential heat flow is neglected;
- the thermal capacitance and heat generation are uniformly distributed;
- radial heat flow is defined by a single mean temperature.

The thermal resistances for a cylindrical component are calculated as proposed by Mellor [9]. The thermal network for the component considered is a three terminals network, as shown in Figure 54.

Θ_1 and Θ_2 are the internal and external surface temperatures, θ_m is the mean temperature, i.e. the interesting point. In case of no-internal heat generation, the central point of the cylindrical wall (between R_1 and R_2) has a temperature equal to Θ_m .

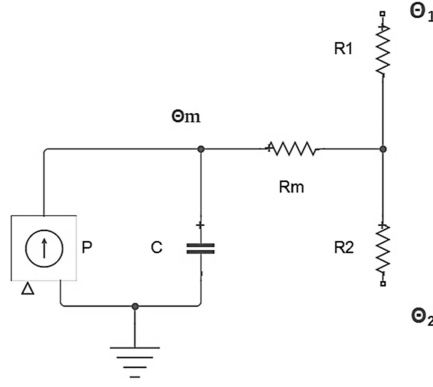


Figure 54 Thermal network-cylindrical component

R_1 and R_2 are the thermal resistances in the radial directions and R_m is the radial interconnecting resistance. In presence of internal heat generation, the mean temperature is lower than the temperature given by the central node and for this reason it is used a negative thermal resistance R_m .

Assuming the stator yoke, the permanent magnet, the rotor and the shaft as a cylindrical component, the thermal resistances are defined by:

$$R_1 = \frac{1}{2\pi\lambda_r L} \left(1 - \frac{2r_2^2 \ln\left(\frac{r_1}{r_2}\right)}{r_1^2 - r_2^2} \right)$$

$$R_2 = \frac{1}{2\pi\lambda_r L} \left(\frac{2r_2^2 \ln\left(\frac{r_1}{r_2}\right)}{r_1^2 - r_2^2} - 1 \right) \quad (75)$$

$$R_m = -\frac{1}{4\pi(r_1^2 - r_2^2)\lambda_r L} \left(r_1^2 + r_2^2 - \frac{4r_2^2 \ln\left(\frac{r_1}{r_2}\right)}{r_1^2 - r_2^2} \right)$$

Where r_1 and r_2 are respectively the outer and inner diameter of the hollow cylinder, L is the length and λ_r is the radial conductive coefficient.

The thermal capacitance for a generic cylindrical component is given by:

$$C = \rho c \pi (r_1^2 - r_2^2) L \quad (76)$$

Where ρ is the material density.

4.3 Lumped Parameter Thermal Network

Figure 55 shows the eight-node thermal network employed to model the motors.

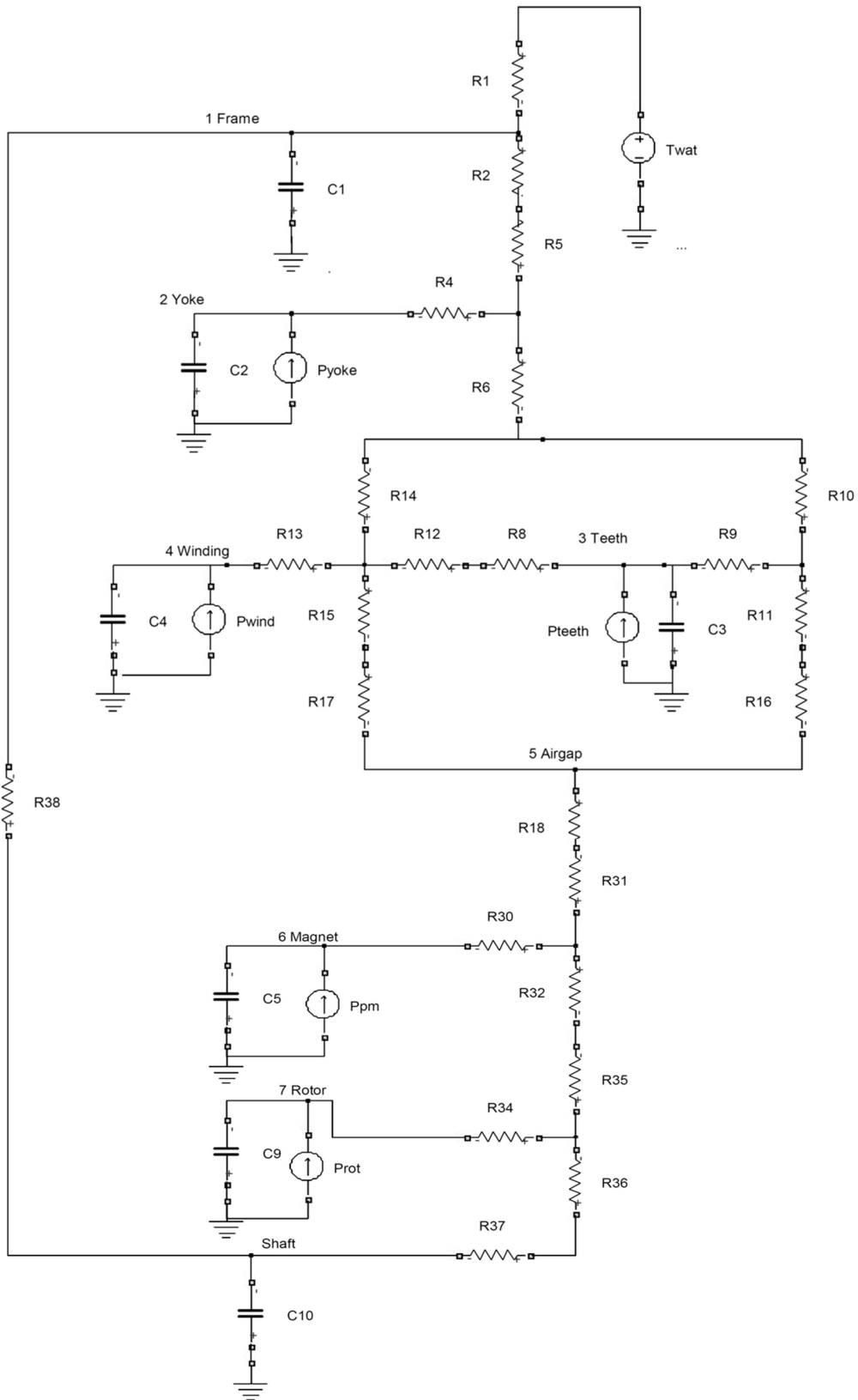


Figure 55 Thermal network

Where the all components are explained in the Table 28.

Thermal Resistance	Explanation
R ₁	Thermal resistance between coolant and frame
R ₂	Thermal resistance between frame and yoke
R ₄	Interconnecting thermal resistance of the yoke
R ₅	Thermal resistance from yoke to frame
R ₆	Thermal resistance from the yoke to teeth
R ₈	Thermal resistance from teeth to stator
R ₉	Interconnecting thermal resistance of the teeth
R ₁₀	Thermal resistance from teeth to yoke
R ₁₁	Thermal resistance from teeth to yoke
R ₁₂	Radial/circumferential thermal resistance from windings to stator
R ₁₄	Thermal resistance from windings to yoke
R ₁₅	Thermal resistance from windings to airgap
R ₁₆	Thermal resistance from the airgap to teeth
R ₁₇	Thermal resistance from the airgap to windings
R ₁₈	Thermal resistance from airgap to magnet
R ₃₀	Interconnecting thermal resistance of magnets
R ₃₁	Thermal resistance from the magnets to airgap
R ₃₂	Thermal resistance from the magnets to rotor
R ₃₄	Interconnecting thermal resistance of rotor
R ₃₅	Thermal resistance from the rotor to the magnets
R ₃₆	Thermal resistance from the rotor to shaft
R ₃₇	Thermal resistance from the shaft to the rotor
R ₃₈	Thermal resistance from the shaft to frame through bearings

Table 28 Component explanation of the thermal network

4.3.1 Frame and Cooling Jacket

The frame is composed of a cooling jacket, which is the reference temperature of the model. Water flows through the cooling jacket.

Table 29 summarizes the water physical properties for different temperatures. It is considered a temperature value for the water of 40°C.

The design of the cooling jacket consists of two rectangular channels. The contact surface of the cooling jacket and stator (S_{cj}) is determined by the outer diameter of the stator (r_1), the width (w_{ch}) and the number of cooling channels (N_{ch}), as shown in Eq.(77).

$$S_{cj} = 2\pi r_1 N_{ch} w_{ch} \quad (77)$$

Temperature	Density	Specific heat	Thermal conductivity	Cinematic viscosity	Dynamic viscosity
Θ_w (°C)	ρ_{wa} kg/m ³	c_{pwa} J/(kg K)	λ_{wa} W/(m K)	ν_{wa} m ² /s	μ_{wa} (Pa s)
20	998	4182	0.598	$1.01 \cdot 10^{-6}$	$1.002 \cdot 10^{-3}$
40	992	4178	0.627	$0.66 \cdot 10^{-6}$	$0.653 \cdot 10^{-3}$
60	983	4194	0.652	$0.48 \cdot 10^{-6}$	$0.467 \cdot 10^{-3}$

Table 29 Physical properties of water at different temperatures

The hydraulic diameter is determined by the rectangular channel section (A_{ch}) and the channel perimeter (P_{ch}).

$$d_{hyd} = \frac{4w_{ch}h_{ch}}{2(w_{ch}+h_{ch})} = 4 \frac{A_{ch}}{P_{ch}} \quad (78)$$

Figure 56 shows the cross section of the frame, with a detail of the channels size on right.

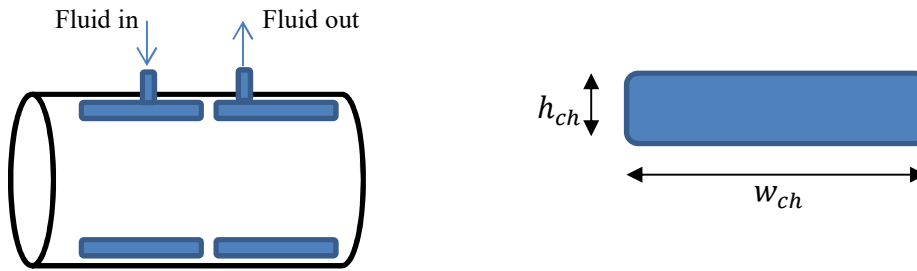


Figure 56 Cooling channel

The speed of fluid inside the channel is given by:

$$s_{wa} = \frac{Q}{A_{ch}} \quad (79)$$

Where Q is the mass flow rate (kg/m^3).

The convective coefficient in this surface is given by the equation:

$$\alpha_{ch} = Nu \frac{k_w}{d_{hyd}} \quad (80)$$

Where the *Nusselt* number (Nu) depends on the fluid motion and k_w is the water thermal conductivity. The fluid motion is laminar or turbulent, and it is defined by *Reynolds* number (Re):

$$Re = \frac{\rho_{wa} s_{wa} d_{hyd}}{\mu_{wa}} \quad (81)$$

For a value below 3000, the motion is considered laminar and the Nusselt number is given by Eq.(82) [15]:

$$Nu = 7.49 - 17.02 \frac{h_{ch}}{w_{ch}} + 22.43 \left(\frac{h_{ch}}{w_{ch}}\right)^2 - 9.94 \left(\frac{h_{ch}}{w_{ch}}\right)^3 + \frac{0.065 \left(\frac{d_{hyd}}{P_{ch}}\right) Re Pr}{1 + 0.04 \left(\left(\frac{d_{hyd}}{P_{ch}}\right) Re Pr\right)^{\frac{2}{3}}} \quad (82)$$

Pr is the *Prandtl* number defined by:

$$Pr = c_{pwa} \frac{\mu}{k} \quad (83)$$

If *Reynolds* value is above 3000, the motion is turbulent and the *Nusselt* number is given by:

$$Nu = \frac{f}{8} \frac{(Re - 1000) Pr}{1 + 12.7 \left(\frac{f}{8}\right)^{0.5} (Pr^{2/3} - 1)} \quad (84)$$

Where f is the friction factor. For a smooth wall it is [15]:

$$f = [0.790 \ln(Re) - 1.64]^{-2} \quad (85)$$

Finally, the resistance between cooling jacket and frame can be calculated by:

$$R_1 = \frac{1}{\alpha_{ch} S_{cj}} \quad (86)$$

In the Table 30 all parameter are shown in the case of $Q=8$ l/min.

Parameter	Symbol	Value
Channel Number	N_{ch}	2
Channel width	w_{ch}	65 mm
Channel height	h_{ch}	6 mm
Channel Area	A_{ch}	390 mm ²
Channel Perimeter	P_{ch}	142 mm ²
Hydraulic diameter	d_{hyd}	10.9 mm
Fluid speed	s_{wa}	0.427 m/s
Reynold Number	Re	5706
Prandtl Number	Pr	4.351
Convective coefficient	α_{ch}	2220.2 W/(m ² K)

Table 30 Fluid dynamic parameter of Cooling Jacket

The heat transfer between frame and stator core depends on the contact surface between the parts. A no perfect contact between the surfaces is given by the roughness of the solid parts. This factor is modelled as an equivalent air-gap convection and the thermal resistance is calculated by:

$$R_2 = \frac{1}{\pi \lambda_{cont} r_1}$$

Where r_1 is the outer radius of the stator and λ_{cont} is the frame-yoke contact coefficient. The equivalent air-gap and the thermal conductivity of the contact are [7]:

- Joint equivalent air gap: 0.03-0.04 mm
- $\lambda_{cont} = 650-870 \text{ W}/(\text{m}^2 \text{ K})$

The thermal capacitance is given by:

$$C_1 = \frac{1}{2} M_f c_{al}$$

Where M_f and c_{al} are respectively the frame mass and the specific heat of the aluminium

Parameter	Value
M_f	4.665 kg
c_{al}	910 J/(kg K)
λ_{cont}	800 W/(m ² K)

4.3.2 Stator Yoke

The stator yoke is composed with electrical sheets with a lamination factor s equal to 0.97. In this case, the equation for the calculation of the thermal resistances (Eq. (75)) became the following:

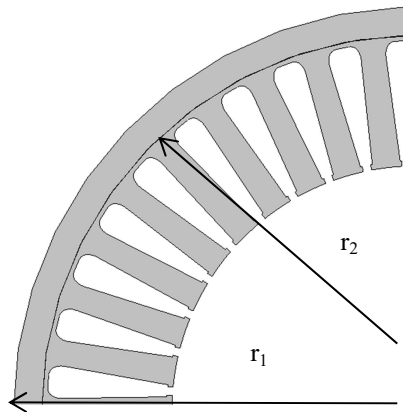


Figure 57 Stator yoke

$$R_4 = -\frac{1}{4\pi(r_1^2 - r_2^2)\lambda_{ir}SL} \left(r_1^2 + r_2^2 - \frac{4r_2^2 r_1^2 \ln\left(\frac{r_1}{r_2}\right)}{r_1^2 - r_2^2} \right)$$

$$R_5 = \frac{1}{2\pi\lambda_{ir}SL} \left(1 - \frac{2r_2^2 \ln\left(\frac{r_1}{r_2}\right)}{r_1^2 - r_2^2} \right)$$

$$R_6 = \frac{1}{2\pi\lambda_{ir}sL} \left(\frac{2r_2^2 \ln\left(\frac{r_1}{r_2}\right)}{r_1^2 - r_2^2} - 1 \right)$$

The thermal capacitance is given by:

$$C_2 = \frac{c_{ir}\rho_{ir}\pi Ls(r_1^2 - r_2^2)}{2}$$

Where c_{ir} is the lamination iron specific heat and ρ_{ir} the lamination iron density, listed in Table 31.

Parameter	Symbol	Value
NO20 radial thermal conductivity	λ_{ir}	28 W/(m K)
NO20 specific heat	c_{ir}	1900 J/(kg K)
NO20 density	ρ_{ir}	7650 kg/m ³
Lamination stacking factor	s	0.97

Table 31 NO20 physical proprieties

4.3.3 Stator Teeth

The stator teeth can be considered as a group of cylindrical segments connected thermally in parallel. For the calculation of the thermal resistances, the tooth width ϕ_w and the tooth pitch ϕ_p (circumferential distance between two consecutive teeth) are needed. In addition, the circumferential heat flow from the slot windings to the teeth (R_9) is considered.

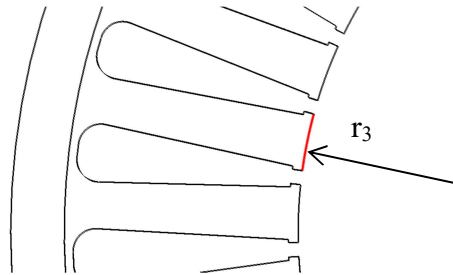


Figure 58 Stator teeth

$$R_8 = \frac{\pi\phi_w(r_2^2 - r_3^2)}{\lambda_r Ls\phi_p(r_2^2 - r_3^2)^2 n^2}$$

$$R_9 = -\frac{\phi_p}{4\pi(r_2^2 - r_3^2)\lambda_r sL\phi_w} \left(r_2^2 + r_3^2 - \frac{4r_2^2 r_3^2 \ln\left(\frac{r_2}{r_3}\right)}{r_2^2 - r_3^2} \right)$$

$$R_{10} = \frac{\phi_p}{2\pi\lambda_r s L \phi_w} \left(1 - \frac{2r_3^2 \ln\left(\frac{r_2}{r_3}\right)}{r_2^2 - r_3^2} \right)$$

$$R_{11} = \frac{\phi_p}{2\pi\lambda_r s L \phi_w} \left(\frac{2r_3^2 \ln\left(\frac{r_2}{r_3}\right)}{r_2^2 - r_3^2} - 1 \right)$$

The thermal capacitance is given by:

$$C_3 = \frac{c_{ir} \rho_{ir} \pi L s \phi_w (r_2^2 - r_3^2)}{2\phi_p}$$

4.3.4 Stator Winding

A stator slot is composed of copper, varnish and insulation lining as shown in Figure 59 [16]. The slots are modelled as a group of cylinder connected thermally in parallel. The equivalent shape is made of a copper cylinder with an equivalent radius (r_4) and it is covered by a layer of insulant. The geometrical data regarding the winding is exposed in chapter 2.2.

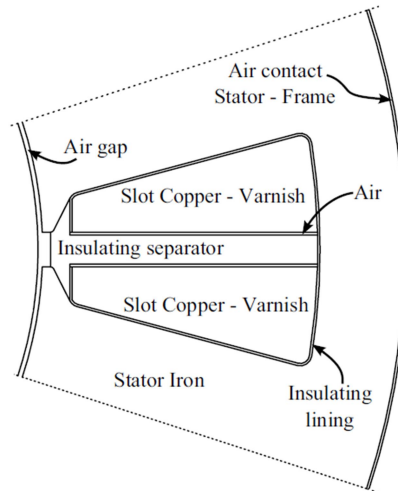


Figure 59 Detail of stator slot

$$r_4 = \sqrt{\frac{S_{slot}}{\pi}} \quad (87)$$

The insulant thickness is listed in Table 5. The equivalent thermal conductivity is given by the following relation as suggested by [9]:

$$\lambda_{cu-v} = F \lambda_v$$

As shown in [16] the radial conductivity F depends on the ratio between the copper diameter and the varnish-insulated diameter.

$$F = 37.5 \left(\frac{d_c}{d_{ins}} \right)^2 - 43.75 \left(\frac{d_c}{d_{ins}} \right) + 14 \quad (88)$$

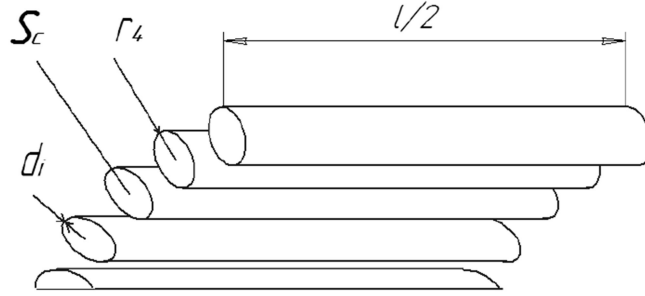


Figure 60 Equivalent stator winding

$$R_{12} = \frac{2d_i}{\pi\lambda_i L r_4 N} + \frac{1}{2\pi\lambda_{cu-v} L N}$$

$$R_{14} = \frac{4d_i}{\pi\lambda_i L r_4 N} + \frac{1}{\pi\lambda_{cu-v} L N}$$

$$R_{15} = \frac{1}{\pi\lambda_{cu-v} L N}$$

Where d_{ins} is the insulant thickness, λ_i is slot liner conductivity, λ_v varnish conductivity and F is radial conductivity factor (2.5) [17].

The thermal capacitance is given by:

$$C_4 = \frac{c_c \rho_c \pi L N \pi r_4^2}{2}$$

Where S_c is the copper cross section in slots.

Parameter	Symbol	Value
Copper conductivity	λ_c	385 W/(m K)
Slot liner conductivity	λ_i	0.21 W/(m K)
Varnish Conductivity	λ_v	0.35 W/(m K)
Copper specific heat	c_c	390 J/(kg K)
Copper density	ρ_c	8960 kg/m ³
	d_c/d_{ins}	0.85
Radial Conductivity	F	3.94

Table 32 Winding thermal proprieties

4.3.5 Airgap

In the airgap, the heat transfer occurs by convection from the stator teeth and the windings to the magnets. *Taylor's* number is introduced to calculate the convective coefficient [18].

$$T_a = \frac{\omega_m^2 r_5 \delta^3}{\nu_{air}} \quad (89)$$

Where r_5 is the outer diameter of the magnets, ν_{air} is the cinematic viscosity of air and ω_m is the angular frequency given by:

$$\omega_m = \frac{(2\pi r_5) n}{60} \quad (90)$$

The convection coefficient is based on the experimental formula given by [19] :

$$\alpha_{air} = Nu \frac{\lambda_{air}}{\delta} \quad (91)$$

According to the Taylor's number, the *Nusselt's* number is determined:

$$Nu = \begin{cases} 2 & T_a < 1700 \\ 0.128 T_a^{0.367} & 1700 < T_a < 10^4 \\ 0.409 T_a^{0.241} & 10^4 < T_a < 10^7 \end{cases} \quad (92)$$

The thermal resistances are given by:

$$R_{16} = \frac{\phi_p}{\phi_w \pi r_3 L \alpha_{air}}$$

$$R_{17} = \frac{\phi_p}{(\phi_p - \phi_w) \pi r_3 L \alpha_{air}}$$

$$R_{18} = \frac{1}{\pi r_5 L \alpha_{air}}$$

In the Table 33 the parameters of the air at 50°C are listed.

Parameter	Symbol	Value
Viscosity	μ	$1.840 \cdot 10^{-5} \text{ kg/(m s)}$
Density	ρ_{air}	1.058 kg/m^3
Specific Heat	c_{air}	1065 J/(kg K)
Thermal conductivity of the air	k_{air}	0.027 W/(m K)
Cinematic viscosity	ν_{air}	$0.0000184 \text{ m}^2/\text{s}$

Table 33 Air physical proprieties at 50°

4.3.6 Permanent Magnets

As already mentioned, the permanent magnets are assumed as a hollow cylinder with outer radius r_5 and inner radius r_6 . Where r_5-r_6 is the magnet's thickness. For simplicity, the layer of insulant around the magnet is neglected.

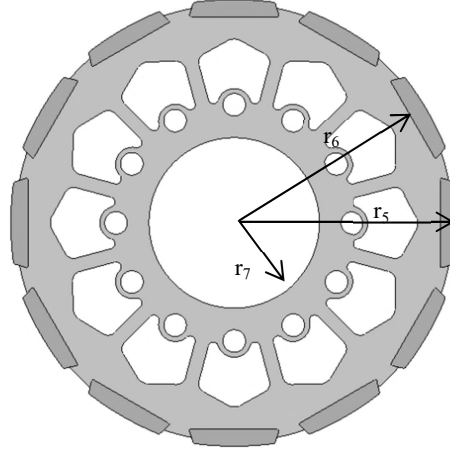


Figure 61 Rotor 2D

The thermal resistance are:

$$R_{30} = -\frac{1}{4\pi(r_5^2 - r_6^2)\lambda_{r_{pm}}L} \left(r_5^2 + r_6^2 - \frac{4r_5^2 r_6^2 \ln\left(\frac{r_5}{r_6}\right)}{r_5^2 - r_6^2} \right)$$

$$R_{31} = \frac{1}{2\pi\lambda_{r_{pm}}L} \left(1 - \frac{2r_6^2 \ln\left(\frac{r_5}{r_6}\right)}{r_5^2 - r_6^2} \right)$$

$$R_{32} = \frac{1}{2\pi\lambda_{r_{pm}}L} \left(\frac{2r_6^2 \ln\left(\frac{r_5}{r_6}\right)}{r_5^2 - r_6^2} - 1 \right)$$

Where $\lambda_{r_{pm}}$ is the thermal conductivity of the Neodymium Iron Boron.

The thermal capacitance is given by:

$$C_8 = \frac{1}{2} \pi \rho_{PM} c_{PM} L (r_5^2 - r_6^2)$$

Parameter	Symbol	Value
NdFeB Conductivity	$\lambda_{r_{PM}}$	9 W/(m K)
NdFeB specific heat	c_{PM}	502 J/(kg K)
NdFeB density	ρ_{PM}	7500 kg/m ³

Table 34 NdFeB physical proprieties

4.3.7 Rotor

The rotor presents 12 holes (m) distributed on the cross section. In order to simplify the model an equivalent hollow cylinder is assumed. The equivalent radius is calculated to give the same area of the original hole-shape, which is measured with the measurement tools of *JMag*.



Figure 62 Hole radius

$$A_{hole} = 1.4077 \cdot 10^{-4} \text{ m}^2$$

$$r_{10} = \sqrt{\frac{A_{hole}}{\pi}} = 0.0067 \text{ m}$$

The same assumption of the stator is used for taking into account the lamination.

The thermal resistances are calculated by [9].

$$R_{34} = -\frac{1}{4\pi(r_6^2 - r_7^2 - mr_{10}^2)\lambda_r sL} \left(r_6^2 + r_7^2 - \frac{4r_6^2 r_7^2 \ln\left(\frac{r_6}{r_7}\right)}{r_6^2 - r_7^2} \right)$$

$$R_{35} = \frac{r_6^2 - r_7^2}{2\pi\lambda_r Ls(r_6^2 - r_7^2 - mr_{10}^2)} \left(1 - \frac{2r_7^2 \ln\left(\frac{r_6}{r_7}\right)}{r_6^2 - r_7^2} \right)$$

$$R_{36} = \frac{r_6^2 - r_7^2}{2\pi\lambda_r sL(r_6^2 - r_7^2 - mr_{10}^2)} \left(\frac{2r_6^2 \ln\left(\frac{r_6}{r_7}\right)}{r_6^2 - r_7^2} - 1 \right)$$

Where r_7 is shaft radius.

The thermal capacitance is given by:

$$C_9 = \frac{1}{2} \pi \rho_r c_r L (r_6^2 - r_7^2 - m r_{10}^2)$$

4.3.8 Shaft

The shaft is modelled as a cylinder with the thermal resistance in radial direction between the shaft and rotor, and the only axial resistance necessary to connect the shaft to the frame.

$$R_{37} = \frac{1}{2\pi\lambda_{ste}L} + \frac{l_m}{2\pi\lambda_{ste}r_9^2}$$

$$R_{38} = \frac{1}{4\pi\lambda_{ste}l_b} + \frac{l_m}{2\pi\lambda_{ste}r_9^2}$$

Where λ_{ste} is the thermal conductivity of the aluminium, l_m is the distance of bearing centre to rotor mean, l_b is the bearing housing width and r_9 is the shaft radius.

In addition, the thermal capacitance:

$$C_{10} = \rho_{ste} c_{ste} \pi r_9^2 \left(l_m + \frac{1}{2} l_b + \frac{1}{6} L \right)$$

Where ρ_{ste} is the steel density and, c_{ste} is the steel specific heat

Parameter	Symbol	Value
Steel Conductivity	λ_{ste}	52 W/(m K)
Steel specific heat	c_{ste}	460 J/(kg K)
Steel density	ρ_{ste}	7700 kg/m ³

Table 35 Shaft physical proprieties

4.4 Steady-State Analysis

In this section, the steady-state analysis is illustrated. The results were carried out through the method of nodal voltage, where in this case, each node represents a temperature.

The temperature rise in the nodes relative to a reference temperature is given by the following formula:

$$[\Delta\Theta] = [G^{-1}][P] \quad (93)$$

P is the vector of the power losses:

$$[P] = \begin{pmatrix} P_1 \\ P_2 \\ P_3 \\ P_4 \\ P_5 \\ P_8 \\ P_9 \\ P_{10} \end{pmatrix} = \begin{pmatrix} 0 \\ P_{yoke} \\ P_{tee} \\ P_{winding} \\ 0 \\ P_{PM} \\ P_{rot} \\ 0 \end{pmatrix}$$

$\Delta\Theta$ is the temperature rise vector

$$[\Delta\Theta] = \begin{pmatrix} \Theta_{frame} \\ \Theta_{yoke} \\ \Theta_{teet} \\ \Theta_{winding} \\ \Theta_{airgap} \\ \Theta_{PM} \\ \Theta_{rot} \\ \Theta_{shaft} \end{pmatrix}$$

G is the thermal conductance matrix, which is defined as:

$$G = \begin{bmatrix} \sum_{i=1}^n \frac{1}{R_{1,i}} & -\frac{1}{R_{1,2}} & \dots & -\frac{1}{R_{1,n}} \\ -\frac{1}{R_{2,1}} & \sum_{i=1}^n \frac{1}{R_{2,i}} & \dots & -\frac{1}{R_{2,n}} \\ \vdots & \vdots & \ddots & \vdots \\ -\frac{1}{R_{n,1}} & -\frac{1}{R_{n,2}} & \dots & \sum_{i=1}^n \frac{1}{R_{n,i}} \end{bmatrix}$$

The overall temperatures can be obtained by adding the reference temperature to the previous formula, as shown in Eq.(94)

$$[\Theta] = [G^{-1}]P + [\Theta_0] \quad (94)$$

Where Θ_0 is a column matrix of the external temperature sources.

A spreadsheet was developed for the steady state analysis. The following parameters were set as input: mechanical speed (n), flow rate, water temperature and the electromagnetic losses.

4.5 Transient Analysis

In the transient analysis, thermal capacitances are introduced to take into account the stored thermal energy in the motor.

The system can be represented by eight first order-coupled differential equations, as shown in Eq.(95)

$$[P] = [G] \left(\theta + [C] \frac{d[\theta]}{dt} \right) \quad (95)$$

Where the temperatures rise vector is given by:

Where C is an 8X8 diagonal matrix:

$$C = \begin{bmatrix} C_1 & 0 & \dots & 0 \\ 0 & C_2 & \dots & 0 \\ \vdots & \vdots & \ddots & \vdots \\ 0 & 0 & \dots & C_n \end{bmatrix} \quad (96)$$

The dynamic response is analogous of an RC electric circuit. Even in this case on the theory, the system achieves the steady-state temperature over an infinite time but in practice, the transient can be assumed finished after 3-4 times the time constant of the system.

4.6 Results

In order to obtain the results, two power loss analysis were carried out. The FE simulations were performed under the following conditions:

- $n=4000$ rpm – current 255 A_{rms} – current phase angle $\beta 90^\circ$

- $n=4000$ rpm – current $255 A_{rms}$ – current phase angle $\beta 110^\circ$

The coolant temperature of 40°C was chosen as a reference temperature and the flow rate was equal to 10 l/m .

The mechanical losses were neglected, since such value is low. However, they could be included as a heat generation in the shaft.

Next the table of results is shown.

Nodes	Power Input (W)	Temperature Θ ($^\circ\text{C}$)	$\Delta\Theta$ ($^\circ\text{C}$)
Frame	0	46.46	6.46
Yoke	70.23	93.39	53.39
Teeth	203.34	111.45	71.45
Winding	806.72	136.28	96.28
Airgap	0	93.95	53.95
PM	8.172	71.60	31.60
Rotor	4.42	69.15	29.15
Shaft	0	54.98	14.98

Table 36 Steady state results ($\beta=90^\circ$)




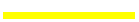



Nodes	Power Input (W)	Temperature $^\circ\text{C}$	$\Delta\Theta$ $^\circ\text{C}$
Frame	0	46.15	6.15
Yoke	53.5	90.67	50.67
Teeth	164.2	107.78	67.78
Copper	806.72	132.95	92.95
Airgap	0	91.95	51.95
PM	7.6	71.20	31.20
Rotor	7.71	68.96	28.96
Shaft	0	54.71	14.71

Table 37 Steady state results ($\beta=110^\circ$)

The transient analysis was carried out with *Dymola* software. It was created an electrical circuit in accord to the thermal network. In this case, the initial voltage of the capacitors represents the reference temperature.

For each node, a voltmeter was used to measure the voltage, namely the temperature.

The following figure show the temperature rise for $\beta=90^\circ$ and for $\beta=110^\circ$.

						
Frame	Yoke	Teeth	Winding	PM	Rotor	Shaft

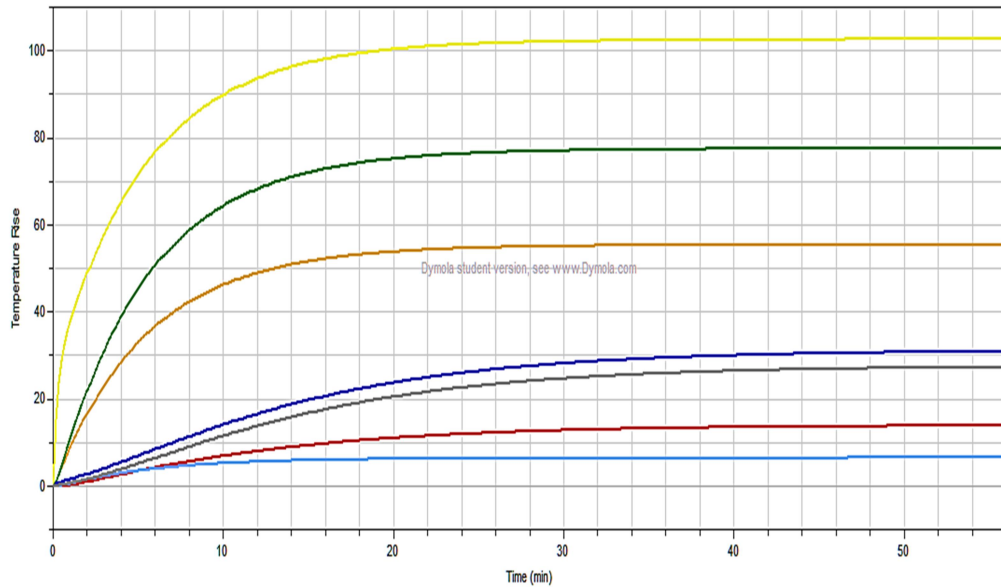


Figure 63 Transient state temperatures ($\beta=90^\circ$)

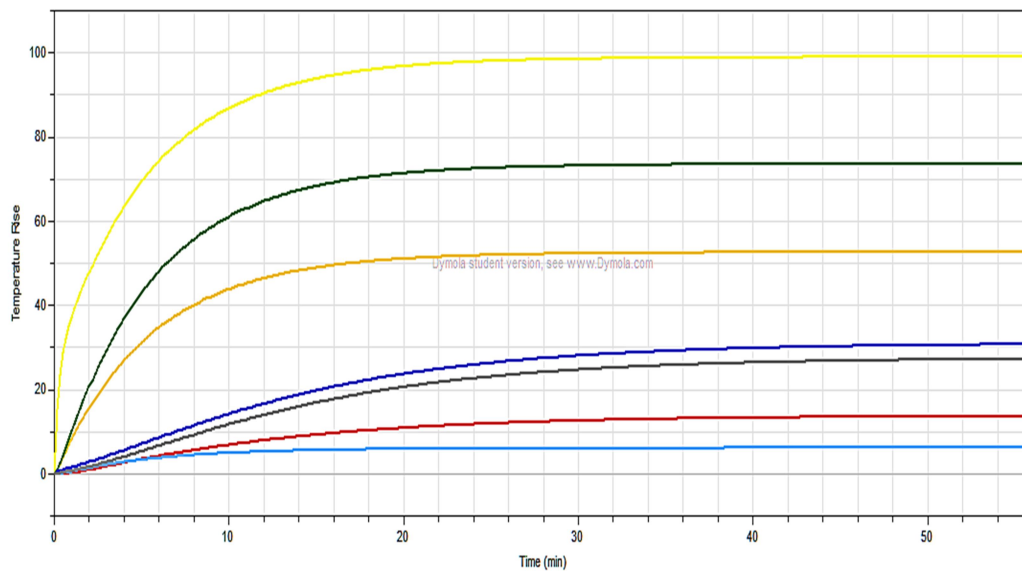


Figure 64 Transient state temperatures ($\beta=110^\circ$)

As shown in Table 36, the hotspot temperature inside of the SPMSM is in the stator winding equal to 136.28 °C.

The temperature in the magnets is quite below the maximum operating temperature (150°C). Table 37 shows that with the increase of current phase angle, a small reduction of temperatures is achieved. Table 38 shows the comparison of the results between the operating point $\beta = 110^\circ$ and the operating point of $\beta = 90^\circ$. Where:

$$\Delta P_l = \frac{P_{110} - P_{90}}{P_{110}}$$

$$\Delta \Theta = \frac{\Theta_{110} - \Theta_{90}}{\Theta_{110}}$$

Nodes	ΔP (W)	$\Delta \Theta$ (°C)	ΔP %	$\Delta \Theta$ %
Frame	0	-0.31	0	-0.67
Yoke	-16.73	-2.72	-31.27	-3.00
Teeth	-39.14	-3.67	-23.84	-3.41
Winding	0	-3.33	0.00	-2.50
Airgap	0	-2	0.00	-2.18
PM	-0.572	-0.4	-7.53	-0.56
Rotor	3.29	-0.19	42.67	-0.28
Shaft	0	-0.27	0.00	-0.49

Table 38 Comparison of temperature results

In detail, the reduction of the magnets temperature is small enough, given for a reduction of the stator losses correspond an increment of the rotor losses, as shown in Table 38.

5 Summary

The aim of the thesis was to reduce the working temperature of the rare earth PMs in order to reduce the amount of dysprosium, since that is used to increase the thermal stability.

In order to achieve this goal, we carried out an electromagnetic analysis coupled with a thermal analysis.

Before starting with the electromagnetic analysis, we designed the configuration of the motor: materials, stator windings layout, electrical and mechanical parameters.

Considering that the number of slots per pole and phase (q) is not an integer and superior to the unit, the design is called fractional-slot winding. We used the “*star of slots*” approach with the purpose to find the balanced and symmetrical design. As shown in the second chapter, the results prove that the chosen configuration achieves the goal.

In the third chapter, we designed the 2D geometry of the motor and we tested the performances in different cases by using the FEM software *JMag*.

By means of the finite-element analysis, we computed the inductance in the direct and quadrature axis.

Afterwards, we performed an iron loss analysis according to the current phase angle. We proved that a negative increment of the direct current causes a reduction of the stator iron losses. We used the procedure of *Doppelbauer* to evaluate the efficiency map of the motor, by analysing the power budget in only seven points.

In the fourth chapter, we created a lumped parameter thermal network through which we compared the thermal behaviour of the machine in accord with the current phase angle. The analysis was performed in the steady state and in the transient state.

The results show a slight diminution of the overall temperature. Moreover, the magnets temperature was quite below the maximum operating temperature and the demagnetization was avoided.

Future researches could be concentrated based on the work presented in this thesis.

First of all the reason of the increment of the rotor losses could be studied through a FEM analysis.

An experimental No-load test is mandatory to prove the winding configuration through the comparison of the no-load voltage.

Regarding the thermal network it is needed a validation of the results through comparison with the results on the test rig.

In addition a sensitivity analysis could be the best approach to understand which are the parameters which influence more the temperature raising. For example it could be evaluated the optimal flow rate in different situations or the influence of the type of cooling fluid or the initial temperature.

Last but not least, the thermal network can be used to estimate the temperatures within the motors during the Fraunhofer LBF drive cycle.

Bibliography

- [1] N. Bianchi, M. Barcaro and S. Bolognani, "Electromagnetic and Thermal Analysis of Permanent Magnet Synchronous Machine," in *Finite Element Analysis - From Biomedical Applications to Industrial Developments*, Dr. David Moratal, 2012, p. 496.
- [2] S.-K. Sul, *Control of electric Machine Drive Systems*, Wiley-IEEE Press, 2011, pp. 128-146.
- [3] L. Alberti and N. Bianchi, "Theory and Design of Fractional-Slot Multilayer Windings," *IEEE Transactions on Industry Applications*, vol. 49, no. 2, pp. 841-849, 2013.
- [4] T. Finker and K. Hameyer, "Computation of iron and eddy-current losses in IPM motors depending on the field weakening angle and current waveform," in *ISEF 2009-XIV Internation Symposium on Electromagnetic Fields*, Arras, France, 2009.
- [5] J. Pyrhönen, T. Jokinen and V. Hrabovcová, *Design of Rotating Eletrical Machines*, John Wiley & Sons, 2013.
- [6] M. Doppelbauer, "Interpolation procedures for the determination of losses and energy efficiency of electrical machines".
- [7] P. Mellor, D. Roberts and D. Turner, "Lumped parameter thermal model for electrical machines of TEFC design," *IEE Proc. B Electr. Power Appl. UK*, vol. 138, no. 5, pp. 205-218, 1991.
- [8] R. Krishnan, *Permanent magnet synchronous and brushless Dc motor drives*, Blacksburg, Virginia: CRC Press, 2010.
- [9] C. Deak, *Modular Permanent-Magnet Synchronous Motors with high Electromagnetic Utilization*, Aachen: Shaker Verlag, 2011.
- [10] A. Binder, "Großgeneratoren und Hochleistungsantriebe," 2014. [Online]. Available: http://www.ew.tu-darmstadt.de/media/ew/vorlesungen_4/
- [11] S. Ruoho, S.-N. Timo , K. Jere , A. Antero and S. Ruoho , "Modeling Magnet Length In 2-D Finite-Element Analysis of Electric Machines," *IEEE Trans. Magn.*, vol. 45, no. 8, pp. 3114-3120 , May 2009.
- [12] M. Doppelbauer, "New Developments in IEC Standards for Motors Driven by frequency Converters".
- [13] D. A. S. a. A. Cavagnino, "Calculations, Convection Heat Transfer and Flow

- Calculations Suitable for Electric Machines Thermal Models,” *IEEE TRANSACTIONS ON INDUSTRIAL ELECTRONICS*, 2008.
- [14] L. A. a. N. B. Massimo Barcaro, “Thermal Analysis of Dual Three-phase Machines Under Faulty Operations,” *IEEE*, pp. 165-171, 2011.
- [15] General Electric Company Research and Developme, Heat transfer and fluid flow data, New York: Schenectady, 1970.
- [16] G. I. Taylor, “Distribution of velocity and temperature between concentric,” *Proceedings of the Royal Society A: Mathematical, Physical and Engineering Sciences*, vol. 159, no. 151, pp. 494-512, 1935.
- [17] K. Becker and J. Kaye, “Measurements of Diabatic Flow in an Annulus With an Inner Rotating Cylinder,” *ASME Journal of Heat Transfer*, pp. 97-104, 1962.
- [18] D.Poli and M.Ceraolo, “Chapter 11: Synchronous machines and drives,” in *Fundamentals of Electric Power Engineering*, IEEE.
- [19] M. J. B. B. P. Andrada, “Power Losses in Outside-Spin Brushless D.C. Motors”.
- [20] C. R.M., *Electric drives and their controls*, Oxford: Clarendon Press, 1995.
- [21] T. M. ., P. J. Andrada P., “Power Losses in Outside-Spin Brushless D.C. Motors”.
- [22] L. Popova, “COMBINED ELECTROMAGNETIC AND THERMAL DESIGN,” 2010.
- [23] J. F. Gieras, *Permanent Magnet Motor Technology*, 3rd ed., 2010.
- [24] N. Bianchi, S. Bolognani, M. Dai Pre’ and G. Grezzani, “Design Considerations for Fractional-Slot Winding Configuration of Synchronous Machines,” *IEEE Transactions on Industry Applications*, vol. 42, no. 4, pp. 997-1006, 2006.
- [25] A. R. Tariq, C. E. Nino-Baron and E. G. Strangas, “Iron and Magnet Losses and Torque Calculation of Interior Permanent Magnet Synchronous Machines Using Magnetic Equivalent Circuit,” *IEEE TRANSACTIONS ON MAGNETICS*, pp. 4073-4080, 46 December 2010.
- [26] T. Lingel, “Magnetic Biasing Techniques for Circulators, Analysis and Design Considerations,” [Online]. Available: <http://de.slideshare.net/tlingel/magnetic-biasing-techniques-for-circulators>.
- [27] J. Widmer, R. Martin and M. Kimiabeigi, “Electric vehicle traction motors without rare earth magnets,” *Sustainable Materials and Technologies*, vol. 3, pp. 7-13, 2015.

Appendix

A Efficiency Map- Matlab Code

```
M=[ 1 0.9 0.81 0.9 0.81 1 1 ;
    1 0.5 0.25 0.5 0.25 1 1;
    1 0.9 0.81 0.225 0.2025 0.5 0.25;
    1 0.5 0.25 0.125 0.0625 0.5 0.25;
    1 0.25 0.0625 0.25 0.0625 1 1;
    1 0.5 0.25 0.03125 0.015625 0.25 0.0625;
    1 0.25 0.0625 0.015625 0.00390625 0.25 0.0625;]
%Input: Power Losses P1(0.9;1) P2(0.5 1) P3(0.9;1) P4(0.5;
0.5) P5(0.25;1) P6(0.5;0.25) P7(0.25;0.25)

P1=845.9077876;
P2=702.9702836;
P3=373.4501697;
P4=245.1029005;
P5=641.2422533;
P6=131.4560453;
P7=76.26193035;
P1= [P1; P2; P3; P4; P5; P6; P7;];

%interpolation coefficient
I=inv(M)*P1;
A=I(1);
B=I(2);
C=I(3);
D=I(4);
E=I(5);
F=I(6);
G=I(7);
%code

for t= 1:35.82

    for f =1:450
        p_m(f,t)=(2*3.14*f*10*t)/60;
        p_loss(f,t)= A+B*(f/450) +C*(f/450)^2
+D*(f/450)*(t/33)^2 +E*(f/450)^2*(t/33)^2+ F*(t/33)
+G*(t/33)^2;
        eta(f,t)=p_m(f,t)/(p_m(f,t)+p_loss(f,t));
        T(f,t)=t;
        rpm(f,t)=f*10;
    end
end

end
```

```

figure
n = 16; % number of contour levels
efficiency_map = contourf(rpm,T,eta,n, 'ShowText', 'on' );
colorbar;
xlabel('\it\Omega}_r [rev/min]')
ylabel('\itT}_e [N*m]')
legend

```

B Thermal Resistances

In the following table is listed the values of thermal resistances and thermal capacitance, referred thermal network of Figure 55.

Resistance	Value [K/W]
R1	0.005915
R2	0.040191
R4	-0.002253
R5	0.006594
R6	0.006937
R8	0.004436
R9	-0.015247
R10	0.040297
R11	0.053368
R12	0.054629
R14	0.109259
R15	0.089676
R16	1.021341
R17	4.176457
R18	0.829771
R30	-0.00831
R31	0.024181
R32	0.025729
R34	-0.0386
R35	0.09196
R36	0.163547
R37	0.23813
R38	0.218142

Capacitance	Value [J/K]
C1	5089.92
C2	1161.666
C3	5562.318
C4	395.7618
C5	134.2725
C9	1251.187
C10	185.4239